

Measurement of primordial non-Gaussianity using the WMAP 5-year temperature skewness power spectrum

Joseph Smidt,^{*} Alexandre Amblard,[†] Paolo Serra,[‡] and Asantha Cooray[§]*Center for Cosmology, Department of Physics and Astronomy, University of California, Irvine, California 92697, USA*

(Received 22 July 2009; published 4 December 2009)

We constrain the primordial non-Gaussianity parameter of the local model f_{NL} using the skewness power spectrum associated with the two-to-one cumulant correlator of cosmic microwave background temperature anisotropies. This bispectrum-related power spectrum was constructed after weighting the temperature map with the appropriate window functions to form an estimator that probes the multipolar dependence of the underlying bispectrum associated with the primordial non-Gaussianity. We also estimate a separate skewness power spectrum sensitive more strongly to unresolved point sources. When compared to previous attempts at measuring the primordial non-Gaussianity with WMAP data, our estimators have the main advantage that we do not collapse information to a single number. When model fitting the two-to-one skewness power spectrum, we make use of bispectra generated by the primordial non-Gaussianity, radio point sources, and lensing-secondary correlation. We analyze Q , V , and W -band WMAP 5-year data using the KQ75 mask out to $l_{\text{max}} = 600$. Using V and W -band data and marginalizing over model parameters related to point sources and lensing-secondary bispectrum, our overall and preferred constraint on f_{NL} is 11.0 ± 23.7 at the 68% confidence level ($-36.4 < f_{\text{NL}} < 58.4$ at 95% confidence). We find no evidence for a nonzero value of f_{NL} even marginally at the 1σ level.

DOI: [10.1103/PhysRevD.80.123005](https://doi.org/10.1103/PhysRevD.80.123005)

PACS numbers: 98.70.Vc, 98.80.-k, 98.80.Bp, 98.80.Es

I. INTRODUCTION

The inflationary paradigm has deservedly become a cornerstone of modern cosmology [1–6]. Inflation solves the flatness, horizon, and monopole problems of the standard big-bang cosmology. Furthermore, inflation is the prevailing paradigm related to the origin of density perturbations that gave rise to the large-scale structure we see today. It posits that a nearly exponential expansion stretched space in the first moments of the early universe and promoted microscopic quantum fluctuations to perturbations on cosmological scales today [7–11]. Inflation makes detailed predictions for key statistical features of these fluctuations. These predictions have now begun to be tested by a range of cosmological observations, including cosmic microwave background (CMB) temperature anisotropy and polarization.

Recent measurements of the CMB with a variety of ground, suborbital, and space-based experiments have provided some of the most stringent tests of inflation (e.g., [12,13]). Specifically among the generic predictions of inflation, recent CMB measurements with the temperature anisotropy power spectrum and polarization have established (1) a nearly flat geometry, (2) a nearly scale-invariant spectrum at large angular scales, (3) adiabatic fluctuations, and (4) superhorizon fluctuations through the temperature-polarization cross spectrum. One major pre-

diction of inflation yet to be verified is the stochastic background of primordial gravitational waves [6,14,15]. While strong limits are expected from Planck [16], a detection of the gravitational wave background is the main focus of a next-generation space-based CMB experiment [17–20].

Some other tests of inflation involve the probability distribution function and isotropy of the density perturbations generated by inflation. In the standard slow-roll inflationary model, the inflaton, the hypothesized scalar field or particle responsible for inflation, fluctuates with a minimal amount of self interactions. In fact, such a small amount of self interactions ensures that the fluctuations are nearly Gaussian and that any non-Gaussianity produced would be too small for detection [21–25]. Non-Gaussianity therefore would be a measure of either interactions of the inflaton [26,27] or any nonlinearities [28,29], and a detection of non-Gaussianity would indicate a violation of slow-roll inflation.

In this spirit, models of non-slow-roll inflation or alternatives to inflation have been proposed to generate large, measurable non-Gaussianities. The curvaton mechanism produces curvature perturbations associated with the fluctuations of a light scalar field whose energy density is zero [30]. The inhomogeneous reheating scenario can produce non-Gaussianity through modulated reheating during the reheating stage [31]. Using multiple inflaton fields that are allowed to interact, those interactions can be used to source non-Gaussianity [32]. Lastly, warm inflation [33], ghost inflation [34], and string theory inspired D acceleration [35] and Dirac-Born-Infeld inflation [36] models also give rise to a large non-Gaussianity (see review in Ref. [37]).

*jsmidt@uci.edu

†amblard@uci.edu

‡pserra@uci.com

§acooray@uci.edu

To connect with observable measurements, the associated non-Gaussianity of the CMB can be described in terms of the second-order correction to the curvature perturbations in position space with

$$\Phi(\mathbf{x}) = \phi_L(\mathbf{x}) + f_{\text{NL}}[\phi_L^2(\mathbf{x}) - \langle \phi_L(\mathbf{x}) \rangle^2], \quad (1)$$

where the non-Gaussianity parameter f_{NL} describes the amplitude of the second-order correction. This form was first suggested by Salopek and Bond [28,38] to describe the non-Gaussianity in primordial perturbations from inflation and has been the subject of experimental constraints using a variety of CMB and large-scale structure data in recent years.

Instead of constraints on the non-Gaussianity parameter in the position space, recent studies make use of the bispectrum involving a three-point correlation function in Fourier or multipole space. The configuration dependence of the bispectrum $B(k_1, k_2, k_3)$ with lengths (k_1, k_2, k_3) that form a triangle in Fourier space can be used to separate various mechanisms for non-Gaussianities, depending on the effectiveness of the estimator used. To summarize the status of the non-Gaussianity measurements, an analysis with WMAP 3-year data first suggested a hint of a non-Gaussianity in the local model with $27 < f_{\text{NL}} < 147$ [95% confidence level (CL)], far above the value of $f_{\text{NL}} < 1$ expected in simple, single field, slow-roll inflation models [39]. The WMAP team's preferred measurement of a non-Gaussianity parameter in 5-year *V*- and *W*-band data is $-9 < f_{\text{NL}} < 111$ (95% CL) [12]. The most recent constraint on f_{NL} comes from studying the WMAP 5-year data with an optimal estimator leading to $-4 < f_{\text{NL}} < 80$ (95% CL) [40]. At the 68% confidence level, with a value of $f_{\text{NL}} = 38 \pm 21$, there is still some marginal evidence for a nonzero value of the non-Gaussianity parameter. If such a result continued to hold with Planck, which increases the precision of the f_{NL} measurement by a factor of 3 to 4, then our simple inflationary picture would need to be revised to include a more complex model.

In this paper, we will pursue a new measurement of the primordial non-Gaussianity parameter with a new estimator that preserves some angular dependence of the bispectrum. On the contrary, the estimators employed by most CMB non-Gaussianity studies, including those by the WMAP team [12], involve a measurement that compresses all information of the bispectrum to a single number called the cross skewness computed with two weighted maps. Such a drastic compression limits the ability to study the angular dependence of the non-Gaussian signal and to separate any confusing foregrounds from the primordial non-Gaussianity. In addition to galactic foregrounds, non-Gaussianity measurements could also be contaminated by unresolved point sources, mainly radio and dusty galaxies, and Sunyaev-Zel'dovich (SZ) clusters, among others [41]. Given the increase in size of CMB data, especially with

Planck, it is also necessary to develop accurate measurement techniques to extract f_{NL} that are unbiased.

Our estimator for non-Gaussianity uses a weighted version of the squared temperature-temperature angular power spectrum [42,43], which we refer to as the skewness power spectrum. This power spectrum extracts information from the bispectrum as a function of the multipole of one triangle length in the harmonic space, while summing all configurations given by the other two side lengths. The difference in spatial dependence based on how the maps are weighted provides ways to separate primordial non-Gaussianity from that of the foregrounds. Here, we account for both point source and lensing bispectra with latter resulting from the correlation of the lensing potential with secondary anisotropies [44,45].

To summarize our main results, after marginalizing over the normalizations of point source and lensing-secondary bispectra, with the combination of *V*- and *W*-band maps, we are able to constrain $f_{\text{NL}} = 11.0 \pm 23.7$ at the 68% confidence level or $-36.4 < f_{\text{NL}} < 58.4$ at the 95% confidence level. We find that f_{NL} is never incompatible with zero at 68% confidence when f_{NL} is estimated in independent bins of width 200 between $2 < l < 600$. We find a significant contribution from unresolved point sources, but failed to detect the lensing-secondary cross-correlations using the two statistics we considered here.

In Sec. II, we review the background theory, and in Sec. III, we review the estimator used and our simulation procedure to compute the uncertainties. In Sec. IV, we discuss our methods for analyzing and simulating data. In Sec. V, we discuss our results. In Sec. VI, we conclude with a summary of our results.

II. THEORY

To begin, we define multipole moments of the temperature map through

$$a_{lm} = \int d\hat{\mathbf{n}} T(\hat{\mathbf{n}}) Y_l^{m*}(\hat{\mathbf{n}}). \quad (2)$$

The angular power spectrum and bispectrum are defined in the usual way such that

$$\langle a_{l_1 m_1}^* a_{l_2 m_2} \rangle = \delta_{l_1 l_2}^D \delta_{m_1 m_2}^D C_{l_1}, \quad (3)$$

$$\langle a_{l_1 m_1} a_{l_2 m_2} a_{l_3 m_3} \rangle = \begin{pmatrix} l_1 & l_2 & l_3 \\ m_1 & m_2 & m_3 \end{pmatrix} B_{l_1 l_2 l_3}. \quad (4)$$

Here, the quantity in parentheses is the Wigner- $3j$ symbol. The orthonormality relation for Wigner- $3j$ symbol implies

$$B_{l_1 l_2 l_3} = \sum_{m_1 m_2 m_3} \begin{pmatrix} l_1 & l_2 & l_3 \\ m_1 & m_2 & m_3 \end{pmatrix} \langle a_{l_1 m_1} a_{l_2 m_2} a_{l_3 m_3} \rangle. \quad (5)$$

The angular bispectrum $B_{l_1 l_2 l_3}$ contains all the information available from the three-point correlation function. For example, the skewness, the pseudocollapsed three-point

function of Ref. [46] and the equilateral configuration statistic of Ref. [47] all can be expressed as linear combinations of the bispectrum terms (see Ref. [29] for explicit expressions and Ref. [48] for an expression relating skewness in terms of the bispectrum).

A. Primordial non-Gaussianity

Here, we focus on the local form of the primordial non-Gaussianity. Using the second-order correction to the curvature perturbations Φ in Eq. (1) and following the derivation in Ref. [38], we write the non-Gaussian (NG) angular bispectrum of temperature anisotropies as

$$B_{l_1 l_2 l_3}^{\text{NG}} = 2I_{l_1 l_2 l_3} \int_0^\infty r^2 dr [\alpha_{l_1}(r) \beta_{l_2}(r) \beta_{l_3}(r) + (\text{Perm.})], \quad (6)$$

where

$$I_{l_1 l_2 l_3} \equiv \sqrt{\frac{(2l_1 + 1)(2l_2 + 1)(2l_3 + 1)}{4\pi}} \begin{pmatrix} l_1 & l_1 & l_3 \\ 0 & 0 & 0 \end{pmatrix}, \quad (7)$$

and r is the comoving radial coordinate.

The two functions in $B_{l_1 l_2 l_3}^{\text{NG}}$ are given by

$$\alpha_l(r) \equiv \frac{2}{\pi} \int k^2 dk g_{Tl}(k) j_l(kr), \quad (8)$$

$$\beta_l(r) \equiv \frac{2}{\pi} \int k^2 dk P_\Phi(k) g_{Tl}(k) j_l(kr). \quad (9)$$

Here, $P_\Phi(k) \propto k^{n_s - 4}$ is the primordial power spectrum of Bardeen's curvature perturbations, and $g_{Tl}(k)$ is the radiation transfer function that gives the angular power spectrum as $C_l = (2/\pi) \int k^2 dk P_\Phi(k) g_{Tl}^2(k)$. In Fig. 1, we show four example cases of $\alpha(r)$ and $\beta(r)$. We generate them using a modified version of the CMBFAST code [49] and for our fiducial cosmological parameter values, consistent with WMAP 5-year best-fit model, as summarized in Table I.

B. Unresolved point sources

In addition to the primordial bispectrum, we also account for the non-Gaussianity generated by unresolved radio point sources. If the sources are Poisson distributed, the bispectrum takes a simple form [38] with

$$B_{l_1 l_2 l_3}^{\text{PS}} = I_{l_1 l_2 l_3} b_{\text{ps}}, \quad (10)$$

where

$$b_{\text{ps}} = g^3(x) \int_0^{S_c} S^3 \frac{dn}{dS} dS, \quad (11)$$

where dn/dS is the number counts of sources, and $g(x)$ maps flux density to thermodynamic temperature with $g(x) = c^2(e^x - 1)^2 / 2k_B \nu^2 x^2 e^x$ with $x = h\nu / k_B T_{\text{CMB}} \approx \nu / 56.84$ GHz. This conversion can be simplified to $g(x) =$

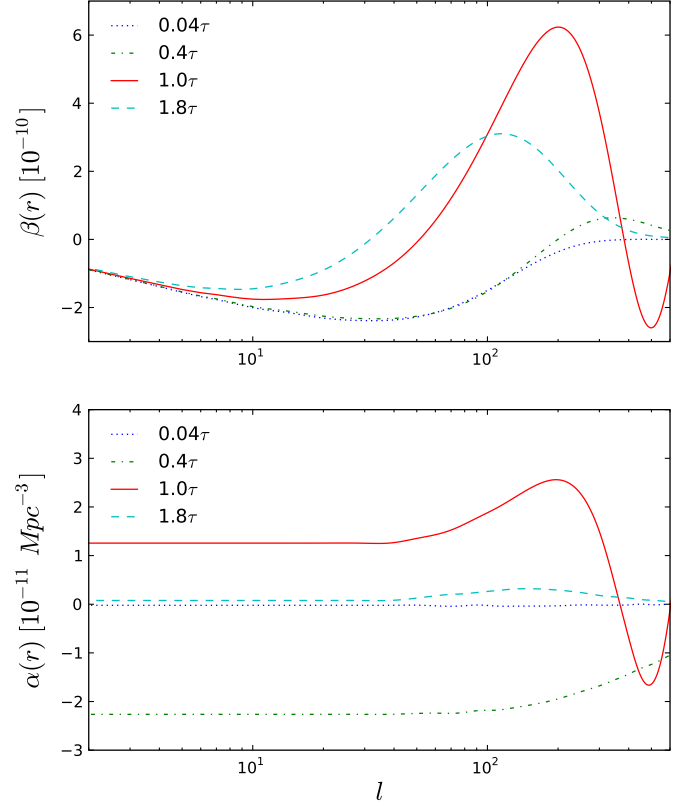


FIG. 1 (color online). $\alpha_l(r)$ and $\beta_l(r)$ with respect to l for r values defined as followed: $r = c(\tau_0 - a\tau)$, where τ_0 is the present day conformal time and $c\tau = 235$ Mpc. In these plots, $a = 0.04, 0.4, 1.0,$ and 1.8 .

$\mu\text{K}/(99.27 \text{ Jy sr}^{-1})(e^x - 1)^2/x^4 e^x$. When model fitting to data, we will ignore the exact number counts of the unresolved sources and parametrize the uncertainty with an overall normalization

TABLE I. Cosmological and noise parameters used in our analysis. The first set is our fiducial cosmology model taken to be consistent with WMAP 5-year best-fit cosmology [12]. The second set of numbers is the normalization parameters related to the instrumental noise in each of the three frequency bands used for the analysis. f_{sky} is the fraction of sky unmasked by KQ75 mask.

Parameter	Value
H_0	71.9 km/s/Mpc
$\Omega_b h^2$	0.02273
$\Omega_c h^2$	0.1099
n_s	0.963
τ	0.087
Δ_R^2	2.41×10^{-9}
σ_0 for Q	2.197 mK
σ_0 for V	3.133 mK
σ_0 for W	6.538 mK
f_{sky}	0.718

$$b_{\text{ps}}^i = A_i \times 10^{-25} \text{ sr}^2, \quad (12)$$

where the index i is for the three bands from WMAP (Q , V , and W) we use here.

Here, we only account for the shot-noise contribution from point sources, similar to the analysis of non-Gaussianity measurements by the WMAP team. It is likely that unresolved point sources are clustered on the sky, though existing WMAP data with measurements at the two-point function level only lead to an upper limit on the clustering amplitude of point sources [50]. In the future, especially for a non-Gaussianity measurement with Planck, it may be necessary to include the bispectrum generated by clustered point sources.

C. CMB lensing-secondary correlation

The gravitational lensing effect of the CMB also generates a bispectrum through correlations of the lensing potential with secondary anisotropies that are generated at late times [44,45,51].

To understand this signal, we note that the lensed temperature fluctuation in a given direction is the sum of the primary fluctuation in a different direction plus the secondary anisotropy

$$\begin{aligned} T(\hat{\mathbf{n}}) &= T^{\text{P}}(\hat{\mathbf{n}} + \nabla\Theta) + T^{\text{S}}(\hat{\mathbf{n}}) \\ &\approx \sum_{lm} [(a_{lm}^{\text{P}} + a_{lm}^{\text{S}})Y_l^m(\hat{\mathbf{n}}) + a_{lm}^{\text{P}}\nabla\Theta(\hat{\mathbf{n}}) \cdot \nabla Y_l^m(\hat{\mathbf{n}})], \end{aligned} \quad (13)$$

or

$$\begin{aligned} a_{lm} &= a_{lm}^{\text{P}} + a_{lm}^{\text{S}} \\ &+ \sum_{l'm'} a_{l'm'}^{\text{P}} \int d\hat{\mathbf{n}} Y_l^{m*}(\hat{\mathbf{n}}) \nabla\Theta(\hat{\mathbf{n}}) \cdot \nabla Y_{l'}^{m'}(\hat{\mathbf{n}}). \end{aligned} \quad (14)$$

Using the definition of the bispectrum in Eq. (5), we obtain

$$\begin{aligned} B_{l_1 l_2 l_3}^{\text{lens-sec}} &= \sum_{m_1 m_2 m_3} \begin{pmatrix} l_1 & l_2 & l_3 \\ m_1 & m_2 & m_3 \end{pmatrix} \int d\hat{\mathbf{m}} \int d\hat{\mathbf{n}} Y_{l_2}^{m_2*} \\ &\times (\hat{\mathbf{m}}) Y_{l_3}^{m_3*}(\hat{\mathbf{n}}) C_{l_1} \nabla Y_{l_1}^{m_1*}(\hat{\mathbf{m}}) \cdot \langle \nabla\Theta(\hat{\mathbf{m}}) T^{\text{S}}(\hat{\mathbf{n}}) \rangle \\ &+ \text{Perm.}, \end{aligned} \quad (15)$$

where the extra five permutations are with respect to the ordering of (l_1, l_2, l_3) .

Integrating by parts and simplifying further leads to a bispectrum of the form

$$\begin{aligned} B_{l_1 l_2 l_3}^{\text{lens-sec}} &= - \begin{pmatrix} l_1 & l_2 & l_3 \\ 0 & 0 & 0 \end{pmatrix} \sqrt{\frac{(2l_1+1)(2l_2+1)(2l_3+1)}{4\pi}} \\ &\times \left[\frac{l_2(l_2+1) - l_1(l_1+1) - l_3(l_3+1)}{2} C_{l_1} b_{l_3}^{\text{S}} \right. \\ &\left. + \text{Perm.} \right]. \end{aligned} \quad (16)$$

When calculating the CMB lensing potential-secondary anisotropy cross-correlation b_l^{S} , we will include both the integrated Sachs-Wolfe (ISW) and the SZ effects, with the latter modeled using the halo approach [52–54]. We will take the sum of the two effects such that $b_l^{\text{S}} = b_l^{\text{ISW}} + b_l^{\text{SZ}}$. The cross-correlation between the lensing potential and ISW is calculated in the standard way [55,56] for the fiducial Λ cold dark matter cosmological model, using only the linear theory potential. For the lensing-SZ correlation, the linear halo model takes into account the SZ profile obtained analytically in Ref. [57] combined with the halo mass function similar to calculations of the SZ angular power spectrum. When model fitting the data, we will parametrize the overall uncertainty with a parameter η_i for each of the WMAP bands such that $B_{l_1 l_2 l_3}^{\text{lens-sec}} \propto \eta_i$.

While lensing modification to CMB bispectrum alone is not expected to make a significant correction to the non-Gaussianity measurement, analytical calculations of the lensing effect on the CMB bispectrum suggest that the lensing-secondary correlation will be the main contamination to a reliable measurement of the primordial non-Gaussianity parameter [41,58–60]. This includes the lensing-ISW effect, since SZ can be “cleaned out” in multifrequency data such as those expected from Planck [48,61]. It is due to this reason that we include the lensing-secondary correlation here.

III. ESTIMATORS OF f_{NL}

We will now motivate a new estimator for measuring f_{NL} . For this we introduce the squared temperature-temperature angular power spectrum and discuss its use as a probe of the angular bispectrum. We motivate a new estimator by revising the original form in Ref. [42].

Through the expansion of the temperature

$$T(\hat{\mathbf{n}}) = \sum a_{lm} Y_l^m(\hat{\mathbf{n}}), \quad (17)$$

we can write

$$a_{lm}^2 = \int d\hat{\mathbf{n}} T^2(\hat{\mathbf{n}}) Y_l^{m*}(\hat{\mathbf{n}}). \quad (18)$$

We emphasize here that a_{lm}^2 denotes the multipole moments of the temperature squared map and not the square of the multipole moments of the temperature map.

We can now construct the angular power spectrum of squared temperature and temperature as

$$C_l^{2-1} = \frac{1}{2l+1} \sum_m a_{lm}^2 a_{lm}^*. \quad (19)$$

After some tedious, but straightforward algebra, we can write the relation between the bispectrum of the temperature field and the angular power spectrum of squared temperature and temperature as

$$C_l^{2^{-1}} = \frac{1}{2l+1} \sum_{l_1 l_2} B_{l_1 l_2 l} \begin{pmatrix} l_1 & l_2 & l \\ 0 & 0 & 0 \end{pmatrix} \times \sqrt{\frac{(2l_1+1)(2l_2+1)(2l+1)}{4\pi}}. \quad (20)$$

Here, we have made use of the relation

$$\sum_{m_1 m_2} \begin{pmatrix} l_1 & l_2 & l \\ m_1 & m_2 & m \end{pmatrix} \begin{pmatrix} l_1 & l_2 & l' \\ m_1 & m_2 & m' \end{pmatrix} = \frac{\delta_{l'l}^D \delta_{mm'}^D}{2l+1}. \quad (21)$$

As it is clear, $C_l^{2^{-1}}$ sums up all triangle configurations of the bispectrum at each of the side lengths l of the triangle in multipolar space.

If *a priori* known that certain triangular configurations contribute to the bispectrum significantly, one can compute this sum by appropriately weighting the multipole coefficients. This is essentially what can be achieved with the introduction of an appropriate weight or a window function in Eq. (18). Though the analytical expression for the two-to-one angular power spectrum involves a sum over the two sides of the angular bispectrum, the experimental measurement is straightforward: one constructs the power spectrum by squaring the temperature field, in real space, and using the Fourier transforms of squared temperature values and the temperature field, with any weighting as necessary.

This simple form of the skewness power spectrum has already been used by Szapudi and Chen [62] to constrain $f_{\text{NL}} = 22 \pm 52 (1\sigma)$ with WMAP 3-year data. The form of the skewness power spectrum as written exactly in Eq. (20) is not useful for a primordial non-Gaussianity measurement. We describe how to filter data for a measurement of primordial non-Gaussianity below.

A. Skewness estimator

To obtain a more useful form, it is useful to review the form of the skewness statistic employed by the WMAP team, which is originating from Ref. [63]. The skewness statistic makes use of two set of maps of the CMB sky as a function of the radial distance r :

$$A(r, \hat{\mathbf{n}}) \equiv \sum_{lm} Y_{lm}(\hat{\mathbf{n}}) A_{lm}(r), \quad (22)$$

$$B(r, \hat{\mathbf{n}}) \equiv \sum_{lm} Y_{lm}(\hat{\mathbf{n}}) B_{lm}(r), \quad (23)$$

where

$$A_{lm}(r) \equiv \frac{\alpha_l(r)}{C_l} b_l a_{lm}, \quad (24)$$

$$B_{lm}(r) \equiv \frac{\beta_l(r)}{C_l} b_l a_{lm}. \quad (25)$$

Here, $C_l \equiv C_l b_l^2 + N_l$ where b_l are the frequency dependent beam transfer functions, and N_l is the power spectrum

from associated simulated noise maps. We discuss both of these quantities later.

In A and B maps, weights are such that they are constructed from the theoretical CMB power spectrum C_l under the assumed cosmological model, the experimental beam b_l , and the primordial non-Gaussianity projection functions $\alpha_l(r)$ and $\beta_l(r)$, where $\alpha_l(r)$ and $\beta_l(r)$ are defined in Eqs. (8) and (9).

The WMAP team's estimator [63] uses an integration in the radial coordinate to obtain the skewness of the product of the A and B^2 maps

$$S_3 \equiv \int r^2 dr \int d\hat{\mathbf{n}} A(r, \hat{\mathbf{n}}) B^2(r, \hat{\mathbf{n}}). \quad (26)$$

In practice, this skewness is corrected by an additional linear term that corrects approximately the effects of partial sky coverage associated with the mask and nonuniform noise. This term is computed by combining observed map with simulated maps that are Monte-Carlo averaged (see Appendix A of Ref. [12]).

As it is clear from above, S_3 involves a complete compression of data to a single number. While in principle different sources of non-Gaussianities contribute to S_3 with a single number alone, it is impossible to separate out the primordial value from the non-Gaussianities generated by secondary anisotropies and other foregrounds. To some extent, the separation is aided by a different set of maps that are weighted differently than the case of A and B maps.

A map optimized for the non-Gaussianity of the form generated by shot-noise from point sources is the E map:

$$E(\hat{\mathbf{n}}) \equiv \sum_{lm} Y_{lm}(\hat{\mathbf{n}}) E_{lm}(r), \quad (27)$$

where

$$E_{lm}(r) \equiv \frac{b_l}{C_l} a_{lm}. \quad (28)$$

Similar to S_3 , one can also compute a skewness associated with E maps by taking $S_{E^3} = \int d\hat{\mathbf{n}} E^3(\hat{\mathbf{n}})$. The WMAP team used the latter to constrain the normalization of the point source Poisson term with b_{ps} .

B. Revised skewness power spectrum

In order to revise the previously discussed skewness power spectrum, instead of simply integrating over the A and B^2 maps, we extract the multipole moments of the B^2 map and the product AB maps

$$(B^2)_{lm}(r) \equiv \int d\hat{\mathbf{n}} B^2(r, \hat{\mathbf{n}}) Y_{lm}(\hat{\mathbf{n}}), \quad (29)$$

$$(AB)_{lm}(r) \equiv \int d\hat{\mathbf{n}} A(r, \hat{\mathbf{n}}) B(r, \hat{\mathbf{n}}) Y_{lm}(\hat{\mathbf{n}}).$$

These two multipole moments then allow us to write the new skewness power spectrum appropriately weighted in the same manner as the previous skewness estimator [43]:

$$\begin{aligned}
C_l^{2-1} &\equiv (C_l^{A,B^2} + 2C_l^{AB,B}), \\
C_l^{A,B^2} &\equiv \frac{1}{2l+1} \int r^2 dr \left[\sum_m \text{Real}\{A_{lm}(r)(B^2)_{lm}(r)\} \right], \\
C_l^{B,AB} &\equiv \frac{1}{2l+1} \int r^2 dr \left[\sum_m \text{Real}\{B_{lm}(r)(AB)_{lm}(r)\} \right].
\end{aligned} \tag{30}$$

To see how C_l^{2-1} probes the primordial bispectrum, we can write the multipole moments of the squared B map as

$$\begin{aligned}
(B^2)_{lm}(r) &= \sum_{l'm'} \sum_{l''m''} \frac{\beta_{l'}(r)}{C_{l'}} \frac{\beta_{l''}(r)}{C_{l''}} \sqrt{\frac{(2l+1)(2l'+1)(2l''+1)}{4\pi}} \\
&\quad \times \begin{pmatrix} l & l' & l'' \\ 0 & 0 & 0 \end{pmatrix} \begin{pmatrix} l & l' & l'' \\ m & m' & m'' \end{pmatrix} a'_{l'm'} a'_{l''m''}, \tag{31}
\end{aligned}$$

where a'_{lm} are the beam times the observed multipole moments ($b_l a_{lm}$). Note that the observed multipole moments relate to theory moments via another beam factor.

Similarly, the multipole moments of the (AB) product map is

$$\begin{aligned}
(AB)_{lm}(r) &= \sum_{l'm'} \sum_{l''m''} \frac{\alpha_{l'}(r)}{C_{l'}} \frac{\beta_{l''}(r)}{C_{l''}} \sqrt{\frac{(2l+1)(2l'+1)(2l''+1)}{4\pi}} \\
&\quad \times \begin{pmatrix} l & l' & l'' \\ 0 & 0 & 0 \end{pmatrix} \begin{pmatrix} l & l' & l'' \\ m & m' & m'' \end{pmatrix} a'_{l'm'} a'_{l''m''}. \tag{32}
\end{aligned}$$

The C_l^{A,B^2} power spectrum is simply then

$$\begin{aligned}
C_l^{A,B^2} &= \frac{1}{2l+1} \int r^2 dr \sum_m \sum_{l'm'} \sum_{l''m''} \frac{\beta_{l'}(r)}{C_{l'}} \frac{\beta_{l''}(r)}{C_{l''}} \frac{\alpha_l(r)}{C_l} \\
&\quad \times \sqrt{\frac{(2l+1)(2l'+1)(2l''+1)}{4\pi}} \begin{pmatrix} l & l' & l'' \\ 0 & 0 & 0 \end{pmatrix} \\
&\quad \times \begin{pmatrix} l & l' & l'' \\ m & m' & m'' \end{pmatrix} a'_{lm} a'_{l'm'} a'_{l''m''}. \tag{33}
\end{aligned}$$

Using the definition of the angular bispectrum, we can simplify to obtain

$$\begin{aligned}
C_l^{A,B^2} &= \frac{1}{2l+1} \int r^2 dr \sum_{l''m''} \frac{\beta_{l''}(r)}{C_{l''}} \frac{\alpha_l(r)}{C_l} \\
&\quad \times \sqrt{\frac{(2l+1)(2l'+1)(2l''+1)}{4\pi}} \\
&\quad \times \begin{pmatrix} l & l' & l'' \\ 0 & 0 & 0 \end{pmatrix} \hat{B}'_{l'l''} b_l b'_l b''_l, \tag{34}
\end{aligned}$$

where $\hat{B}'_{l'l''}$ is the bispectrum estimated from data under beam smoothing. It relates to the theory bispectrum $B_{l'l''}$ as $\hat{B}'_{l'l''} = B_{l'l''} b_l b'_l b''_l$.

We can similarly simplify the term for $C_l^{AB,B}$ and by putting the two terms together, we find that the total is

$$\begin{aligned}
C_l^{2-1} &\equiv (C_l^{A,B^2} + 2C_l^{AB,B}) \\
&= \frac{1}{(2l+1)} \left[\sum_{l''m''} \left\{ \frac{B_{l'l''}^{\text{NG},f_{\text{NL}}=1} \hat{B}'_{l'l''} b_l b'_l b''_l}{C_l C_{l'} C_{l''}} \right\} \right]. \tag{35}
\end{aligned}$$

If we assume that the observed bispectrum is simply that of the primordial non-Gaussianity, then $\hat{B}'_{l'l''} = \hat{f}_{\text{NL}} B_{l'l''}^{\text{NG}}$ and we can write an estimator for f_{NL} as

$$\hat{f}_{\text{NL}} = (2l+1) C_l^{2-1} / F_{\text{NG,NG}}(l), \tag{36}$$

where $F_{\text{NG,NG}}(l)$ is simply the Fisher matrix element for the primordial bispectrum with $f_{\text{NL}} = 1$:

$$F_{i,j}(l) = \sum_{l''m''} \left\{ \frac{B_{l'l''}^i B_{l'l''}^j}{C_l C_{l'} C_{l''}} \right\}, \tag{37}$$

where now we have redefined noise to be such that $C'_l = C_l + N_l/b_l^2$ as the bispectra are no longer beam smoothed.

In reality, C_l^{2-1} includes contributions from secondary anisotropies and foregrounds. Here, we include the non-Gaussianities generated by point sources and the lensing-secondary correlation. Thus, we write

$$(2l+1) \hat{C}_l^{2-1} = \hat{f}_{\text{NL}} F_{\text{NG,NG}}(l) + \hat{A} F_{\text{NG,PS}} + \hat{\eta} F_{\text{NG,lens-sec}} \tag{38}$$

and consider a joint estimation of the three unknown parameters.

To help break degeneracies between the three parameters, we also estimate the skewness power spectrum of the E map defined in Eq. (27) as

$$C_l^{E,E^2} \equiv \frac{1}{2l+1} \left[\sum_m \text{Real}\{E_{lm}(E^2)_{lm}\} \right]. \tag{39}$$

Similar to our derivation above, one can simplify the multipole moments of the $(E^2)_{lm}$ to show that this probes

$$E_l^{2-1} \equiv C_l^{E,E^2} = \frac{1}{(2l+1)} \left[\sum_{l''m''} \left\{ \frac{B_{l'l''}^{\text{PS},b_{\text{ps}}=1} \hat{B}'_{l'l''} b_l b'_l b''_l}{C_l C_{l'} C_{l''}} \right\} \right]. \tag{40}$$

Thus, we write

$$(2l+1) \hat{E}_l^{2-1} = \hat{f}_{\text{NL}} F_{\text{PS,NG}}(l) + \hat{A} F_{\text{PS,SN}} + \hat{\eta} F_{\text{PS,lens-sec}}. \tag{41}$$

The two Eqs. (38) and (41) will form the main set of equations that we will solve with our measurements. While we have not explicitly stated so far, these two quantities will be measured in 3 WMAP frequency channels making use of Q , V , and W -band data. We allow for frequency dependence in A and η , but assume f_{NL} is the same independent of the frequency in all three channels.

C. Approximate corrections for partial sky

Before we move onto discuss data analysis and our simulations to compute the covariances, we note that we also make a correction to both C_l^{2-1} and E_l^{2-1} to account for partial sky coverage and inhomogeneous noise. This is done in an approximate manner by making use of the equivalent form of the linear terms of the skewness statistic in the language of our skewness power spectrum. For the case of the C_l^{2-1} estimator, the correction is derived in Ref. [43]:

$$C_l^{2-1} = \frac{1}{f_{\text{sky}}} \{C_l^{A,B^2} - 2C_l^{(A,B)B} - C_l^{A,(B^2)}\} + \frac{2}{f_{\text{sky}}} \{C_l^{AB,B} - C_l^{(AB),B} - C_l^{B(A,B)} - C_l^{A(B,B)}\}, \quad (42)$$

where f_{sky} is the sky fraction observed. The new terms are defined as, for example,

$$C_l^{B(A,B)}(r) = \frac{1}{N(2l+1)} \sum_i \sum_m \{(B^D A^S)_l^i(r) (B^S)_l^i(r)\}, \quad (43)$$

where i runs over a set of N simulations, and $(B^D A^S)_l^i$ are the coefficients of spherical harmonics for the map pro-

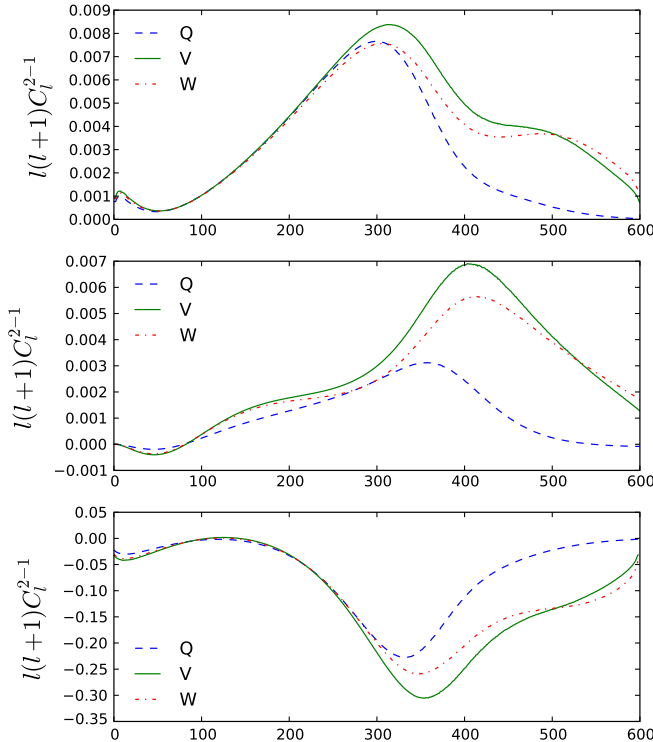


FIG. 2 (color online). Contributions to C_l^{2-1} expected from primordial non-Gaussianity and unresolved point sources. We show the case with $f_{\text{NL}} = 1$ for primordial non-Gaussianity (top), shot-noise from unresolved point sources with $b_{\text{ps}}^i = 1$ (middle), and lensing-secondary signal with $\eta_i = 1$ (bottom).

duced by multiplying the i th simulated A map with the B map derived from raw data.

Similarly, for E_l^{2-1} we find

$$E_l^{2-1} = \frac{1}{f_{\text{sky}}} \{C_l^{E,E^2} - C_l^{E,\langle E^2 \rangle} - 2C_l^{\langle E,E \rangle E}\}, \quad (44)$$

where terms such as $C_l^{E,\langle E^2 \rangle}$ can be written similar to Eq. (43) above with the replacement of E maps instead of A and B maps.

D. Theoretical expectation

In Figs. 2 and 3, we show the theoretical expectations for C_l^{2-1} and E_l^{2-1} , respectively. We plot these for the Q , V , and W band by making use of the beam functions b_l and noise power spectrum estimate N_l that are described in Sec. . Here, we show the cases of primordial non-Gaussianity with $f_{\text{NL}} = 1$, point sources with $A_i = 1$,

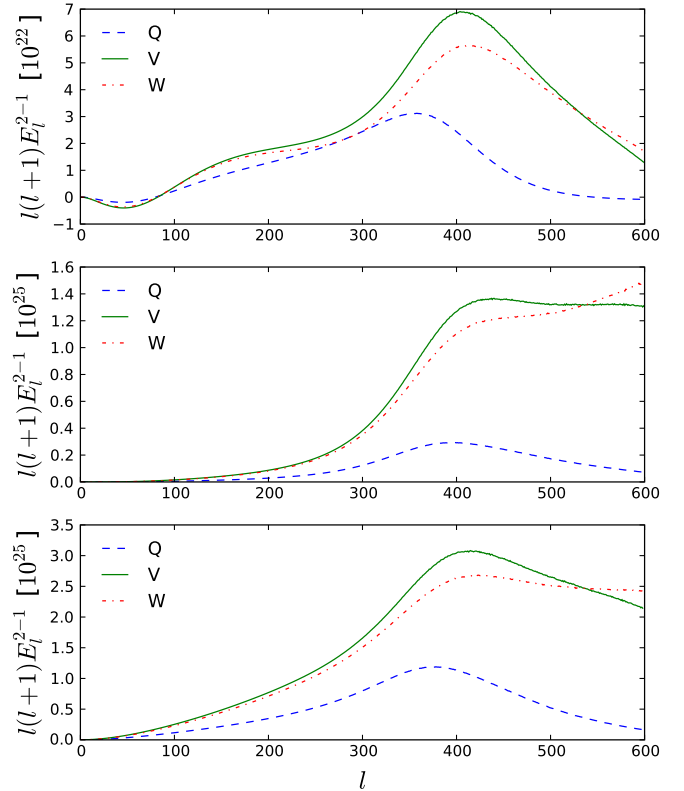


FIG. 3 (color online). Contributions to E_l^{2-1} expected from primordial non-Gaussianity and unresolved point sources. We show the case with $f_{\text{NL}} = 1$ for primordial non-Gaussianity (top), shot-noise from unresolved point sources with $b_{\text{ps}}^i = 1$ (middle), and lensing-secondary signal with $\eta_i = 1$ (bottom). Note the large difference in the y-axis scale from the top curve involving primordial non-Gaussianity to middle and bottom curves with point sources. As is known, the skewness power spectrum associated with E maps is more sensitive to shot-noise bispectrum from point sources.

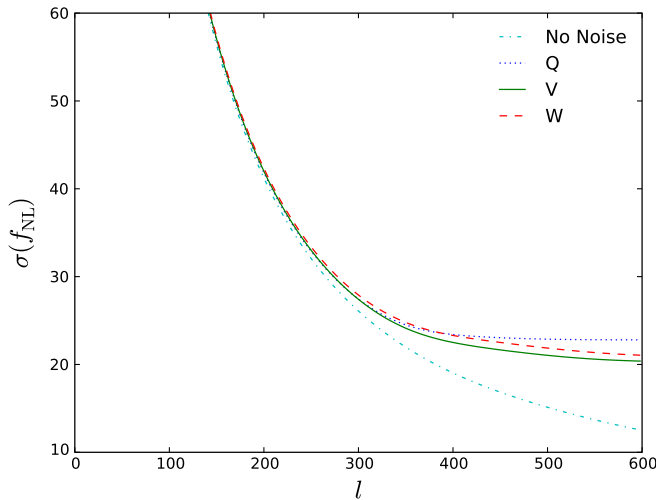


FIG. 4 (color online). Expected error for f_{NL} calculated based on the Fisher matrix approach for each of the three noise curves for the WMAP in Q , V , and W bands and with $f_{\text{sky}} = 0.718$ when using KQ75 mask. The Cramer-Rao bound ranges from about ~ 21 in V band to ~ 23 in Q band. This estimate assumes that only the primordial non-Gaussianity signal is present in the bispectrum and ignores the degeneracies between primordial non-Gaussianity and other parameters, such as those related to unresolved point sources.

and lensing-secondary cross-correlation with b_l^S calculated for the sum of ISW and SZ effects with $\eta_i = 1$.

As it is clear from Fig. 2, the primordial non-Gaussianity signal is expected to be degenerate with foreground non-Gaussianities. The shape of C_l^{2-1} alone is not enough to clearly separate the primordial non-Gaussianity signal from point source and lensing non-Gaussianities. Fortunately, the separation is aided when C_l^{2-1} is combined with E_l^{2-1} . As it is clear from Fig. 3 (especially note the difference in the y axis range for the top and middle plots), this latter power spectrum allows a better determination of the point sources. In practice, we perform a combined analysis of both spectra, including the confusion from secondary bispectra, when model fitting to quantities, f_{NL} , A_i , and η_i . To compare with previous results on the literature related to the non-Gaussianity parameter with WMAP data using the effects of point sources only, we also consider the case where lensing is ignored in the analysis.

In Fig. 4, we include a plot of the $F_{\text{NG,NG}}^{-1/2}(l)$, showing the expected error f_{NL} as a function of the multipole for Q , V , and W bands. Out to l_{max} of 600 and with $f_{\text{sky}} = 0.718$, the Cramer-Rao bound is at the level of ~ 21 with V band to ~ 23 with Q band. This assumes that the bispectrum only contains primordial non-Gaussianity, but the degeneracy between secondary non-Gaussian signals and primordial non-Gaussianity is expected to increase the optimal error at some level more than this bound. Also, to saturate the Cramer-Rao bound, an optimal estimator that accounts

for the mode-mode correlations associated with the partial sky and the mask will become necessary [40]. Our estimator only accounts for the cut-sky approximately making use of the linear terms. We also weight each multipole coefficient with $(C_l b_l^2 + N_l)^{-1}$, as in the case of Gaussian statistics appropriate for the whole sky. While this approach is not different from that of the WMAP team's [12], in an upcoming paper we hope to return to the issue of an exact calculation implementing the full covariance for the two-to-one skewness power spectrum.

IV. DATA ANALYSIS

We first discuss our data analysis procedure and then how we computed the covariance through simulations.

A. Measurement of C_l^{2-1} and E_l^{2-1}

To extract C_l^{2-1} and E_l^{2-1} from data, we use the raw WMAP 5-year Stokes-I sky maps for the Q , V , and W frequency bands as available from the public lambda website.¹ We use Healpix² [64] to analyze the maps. Specifically, starting from the fits files of raw maps, we use *anafast*, masking with the KQ75 mask and without an iteration scheme, to generate multipole coefficients (a_{lm}) for each frequency map out to $l_{\text{max}} = 600$. We will refer to these multipole moments hereafter as a_{lm}^D . With these definitions, we use Eqs. (24), (25), and (28) to generate A_{lm} , B_{lm} , and E_{lm} by substituting a_{lm}^D in place of a_{lm} .

Our recipe for obtaining C_l^{2-1} and E_l^{2-1} is

- (1) Use Healpix and the KQ75 mask to generate a_{lm}^D from the WMAP 5-year Stokes-I sky maps for the Q , V , and W frequency bands.
- (2) Obtain $A(r, \hat{n})$, $B(r, \hat{n})$, and $E(\hat{n})$ from Eqs. (24), (25), and (28) by using $\alpha(r)$ and $\beta(r)$ from Eqs. (8) and (9), respectively, with the replacement of a_{lm} with a_{lm}^D . Figs. 5–7, show the resulting maps.
- (3) Calculate C_l^{A,B^2} , $C_l^{B,AB}$, and the linear terms from Eqs. (30) and (42), respectively, with latter using equations of the form (43). Repeat the same to obtain C_l^{E,E^2} with E maps as defined in Eq. (39) and the corresponding equations for linear terms in Eq. (44). This correction associated with partial sky coverage involves the use of simulated maps described below. We integrate over r from $\tau = 0.004$ to 2 with 500 steps. (see Fig. 1).
- (4) Use the estimated C_l^{2-1} and E_l^{2-1} with WMAP Q , V , and W maps for our parameter estimate analysis (see below).
- (5) Compute analytically F_{ij} terms with $l_{\text{max}} = 600$ in each of the summations of l_1 and l_2 and making use of the noise and beam spectra for WMAP (see below).

¹<http://lambda.gsfc.nasa.gov>

²For more information see <http://healpix.jpl.nasa.gov>

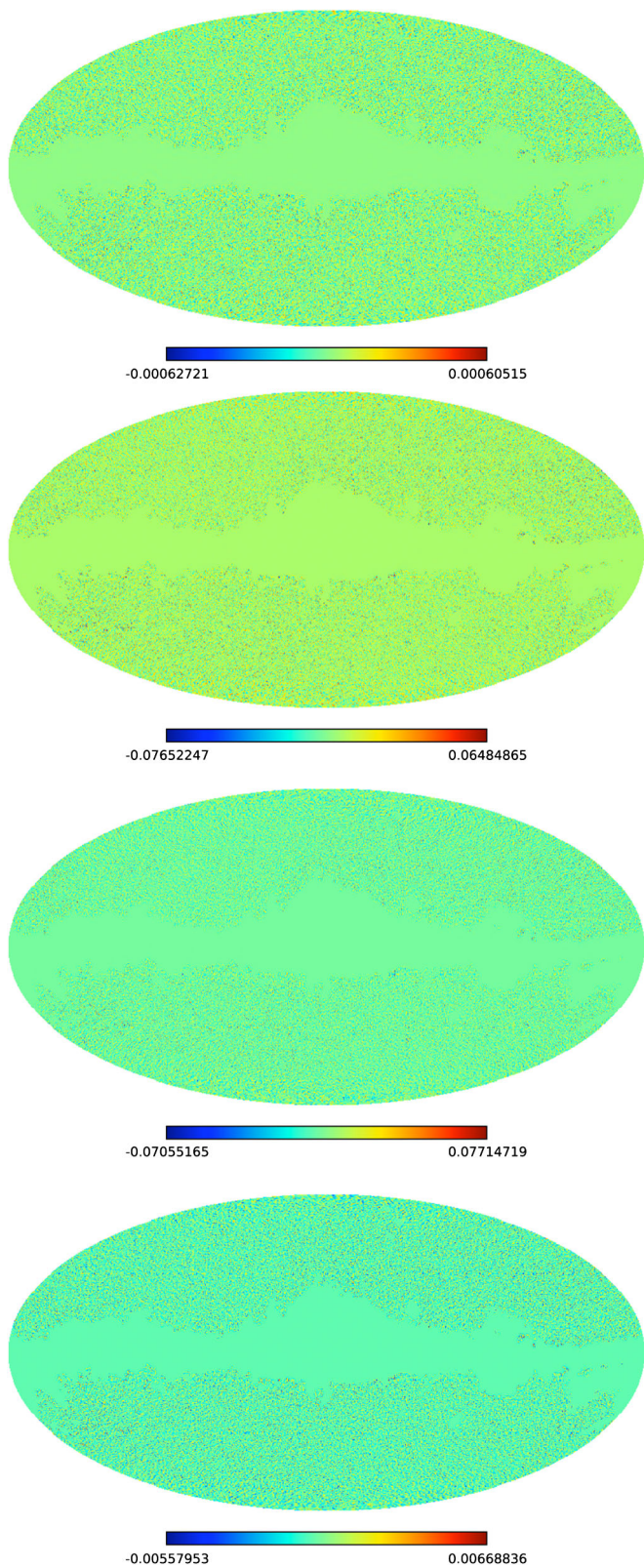


FIG. 5 (color online). *A* maps for *V* frequency band. From upper left hand corner moving clockwise: $\tau = 0.04, 0.4, 1.0, 1.8$.

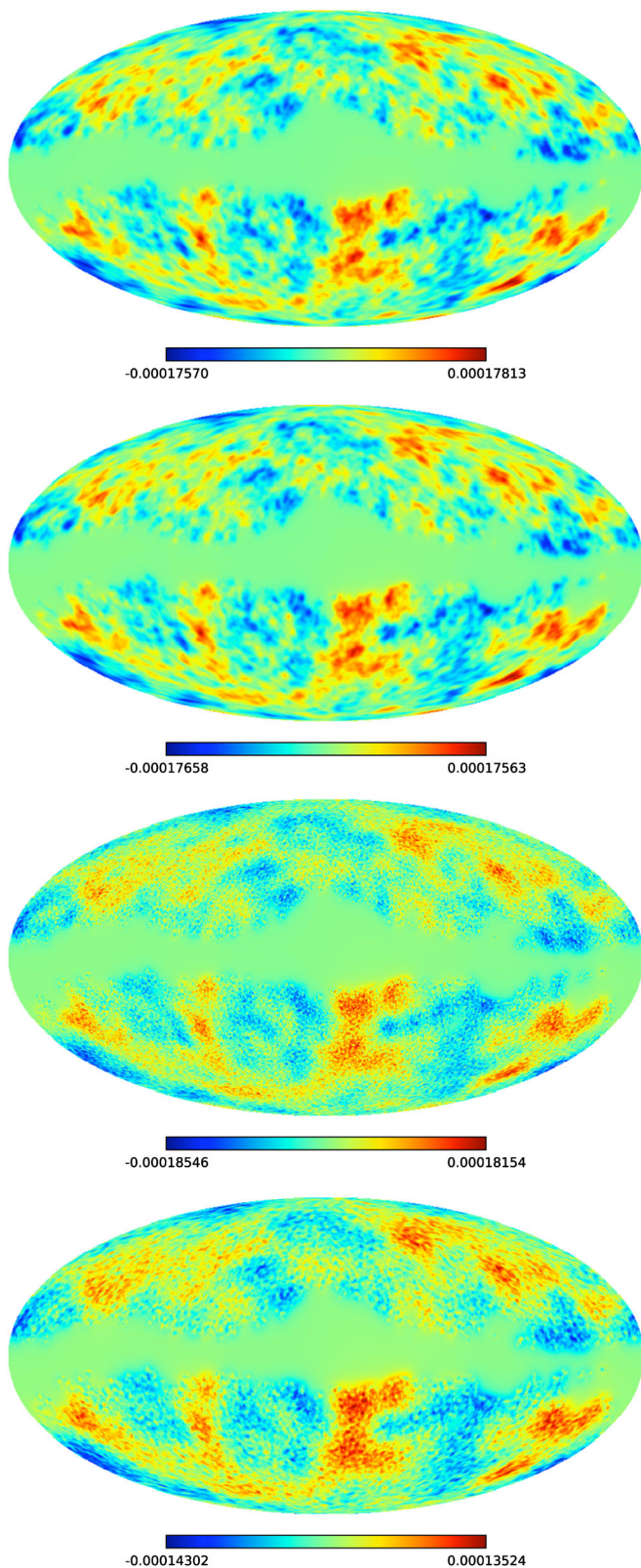


FIG. 6 (color online). *B* maps for *V* frequency band. From upper left hand corner moving clockwise: $\tau = 0.04, 0.4, 1.0, 1.8$.

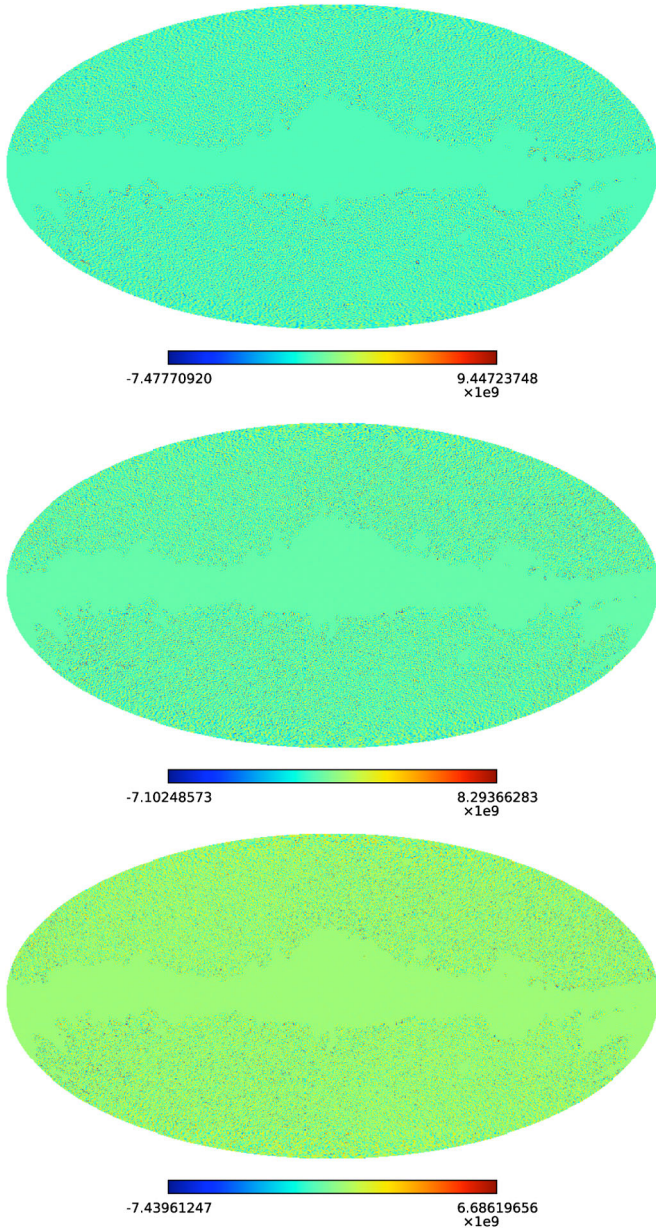


FIG. 7 (color online). E maps for Q , V , and W frequencies.

In Fig. 8, we see the C_l^{2-1} for each WMAP frequency band plotted as a function of l . These plots were generated by binning the estimators with δl of 40 and plotting the midpoint of each bin. The V and W estimators have roughly the same shape and are mostly positive. The Q estimator is noticeably different, dropping negative when $l > 300$.

Furthermore, in Fig. 8, we see E_l^{2-1} for each WMAP frequency band plotted as a function of l . Like the estimators mentioned above, these were similarly binned in bins of size $\delta l = 40$.

Lastly, in Figs. 9 and 10, we see the contributions to C_l^{2-1} and E_l^{2-1} from each term in Eqs. (42) and (44), respectively. The linear terms are not very significant

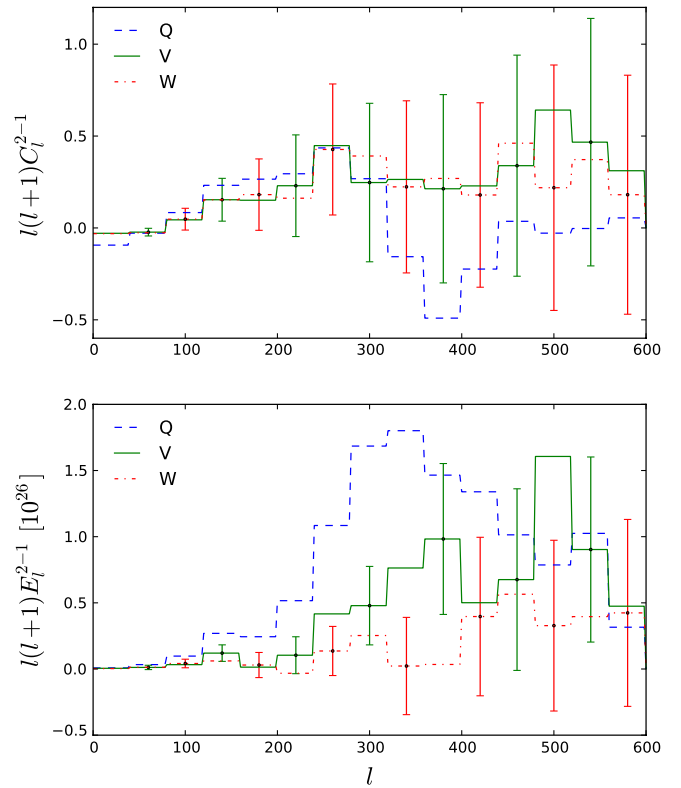


FIG. 8 (color online). C_l^{2-1} (top) E_l^{2-1} (bottom) for Q , V , and W with the measured spectra binned with a width of $\delta l = 40$. The error bars for V and W are also shown.

compared to the other terms. Nevertheless, they are still considered in this analysis.

B. Simulations of A , B , and E maps

In order to do proper statistics for C_l^{2-1} and E_l^{2-1} , we create 250 simulated maps at each WMAP frequency band. To do so, we first produce 250 Gaussian maps to model the CMB sky. For the Gaussian maps, we run the synfast routine of Healpix with an in-file representing the WMAP 5-year best-fit CMB anisotropy power spectrum and generate maps with information out to $l = 600$. We then use anafast, without employing an iteration scheme, masking with the $KQ75$ mask, to produce a_{lm} s for the Gaussian maps out to $l = 600$. We will refer to these a_{lm} s now collectively as a_{lm}^G .

1. Noise

In addition to these Gaussian maps, we create 250 noise maps for each of our frequency bands: Q , V , and W . We generate these maps from white noise with mean = 0 and standard deviation = 1 taking into account σ_0 and N_{Obs} as follows:

$$N(\hat{\mathbf{n}}) = \frac{\sigma_0}{\sqrt{N_{\text{Obs}}}} n(\hat{\mathbf{n}}), \quad (45)$$

where $N(\hat{\mathbf{n}})$ is our noise map, $n(\hat{\mathbf{n}})$ is a map made of pure

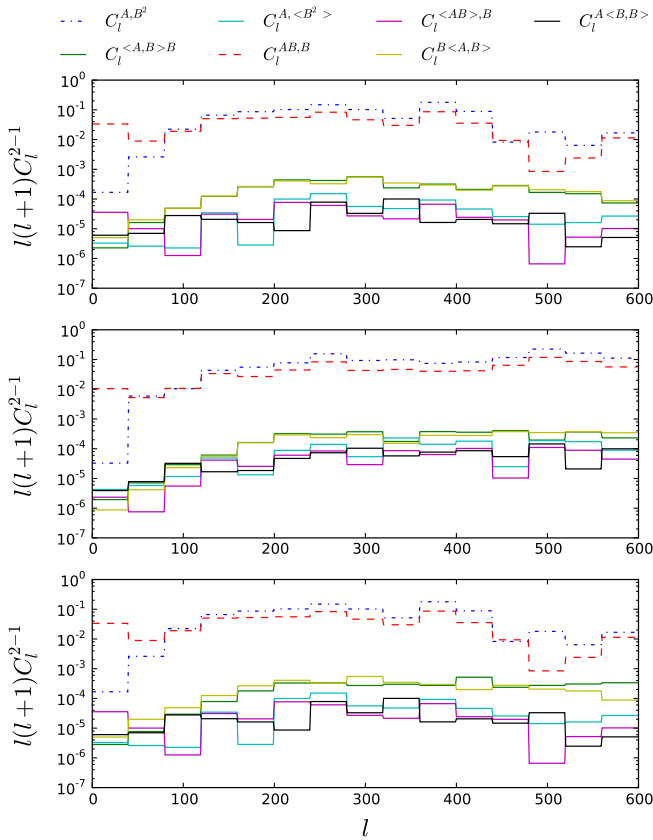


FIG. 9 (color online). Contributions to C_l^{1-2} for Q , V , and W maps.

white noise, N_{obs} is the number of observations per pixel, and σ_0 is the root mean square noise per observation. We use the frequency dependent N_{obs} for each point in the sky provided by the WMAP 5-year Stokes-I map fits files and take $\sigma_0 = 2.197, 3.133,$ and 6.538 mK as established by the WMAP team for Q , V , and W band 5-year data, respectively [65,66]. See also Table I.

Starting with these noise maps, we create alms using anafast with the $KQ75$ mask with no iteration scheme out to $l = 600$. We will henceforth refer to these alms collectively as a_{lm}^N . Furthermore, to calculate the power spectrum from these noise maps, we use Healpix to evaluate the analytical expression

$$N_l = \Omega_{\text{pix}} \int \frac{d^2\hat{\mathbf{n}}}{4\pi f_{\text{sky}}} \frac{\sigma_0^2 M(\hat{\mathbf{n}})}{N_{\text{obs}}(\hat{\mathbf{n}})}, \quad (46)$$

where $\Omega_{\text{pix}} \equiv 4\pi/N_{\text{pix}}$ is the solid angle per pixel, $M(\hat{\mathbf{n}})$ is the $KQ75$ mask, and $f_{\text{sky}} = 0.718$ is the fraction of sky retained by the $KQ75$ mask [12]. Figure 11 shows the power spectrum from our simulated noise maps for each frequency compared to the analytical values quoted by the WMAP 5-year team [12]. For reference, the beam functions b_l^i are plotted in Fig. 12.

To use our estimator on the simulated maps, we must add the noise to the Gaussian maps while at the same time

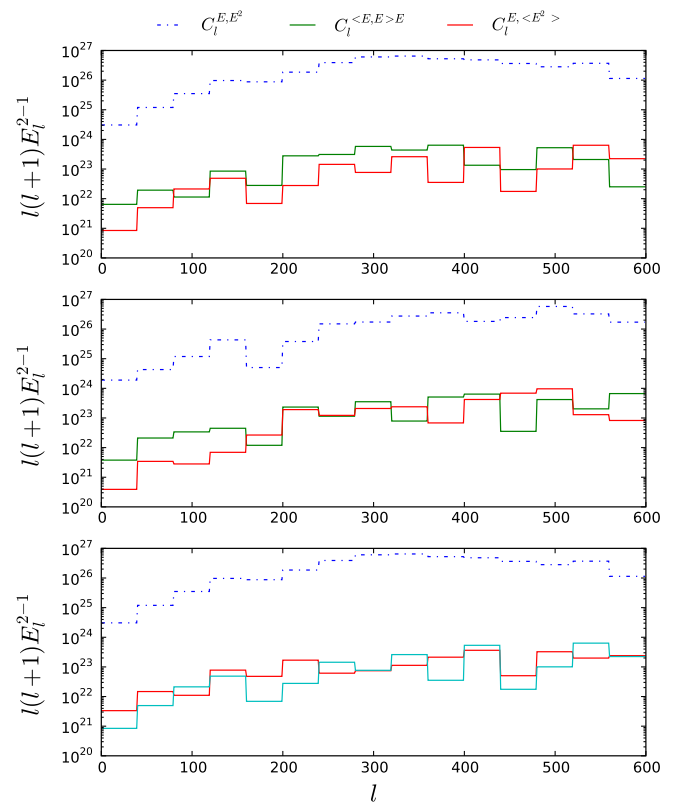


FIG. 10 (color online). Contributions to E_l^{1-2} for Q , V , and W maps.

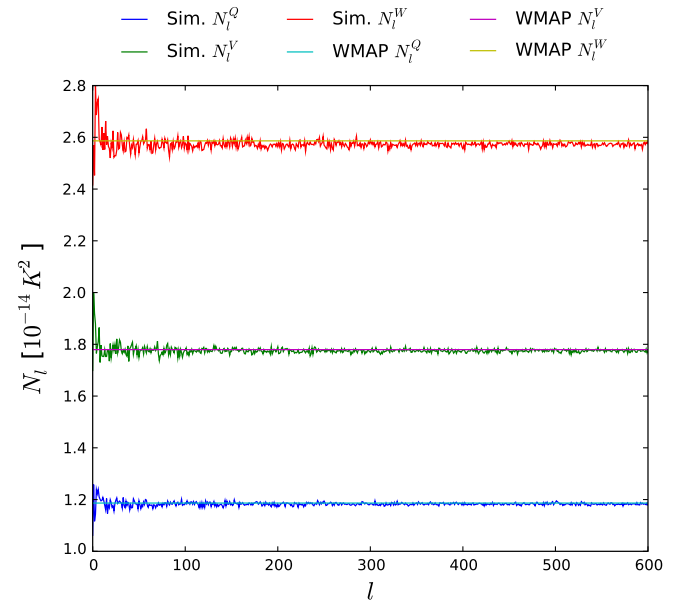


FIG. 11 (color online). The noise power spectrum from our masked simulated noise maps for the Q , V , and W frequency bands compared with the analytical results from the WMAP 5-year team.

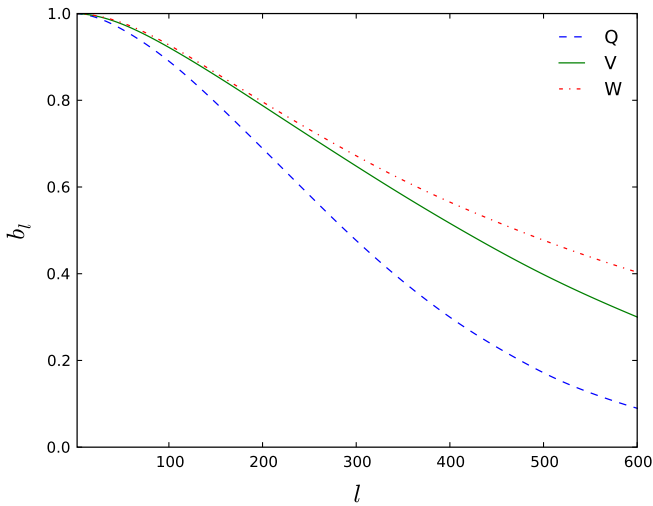


FIG. 12 (color online). The beam transfer functions b_l used in our analysis for each frequency Q , V , and W .

correcting for the beam. To do this, we work in multipole space where we construct the total simulated $a_{lm}^S \equiv a_{lm}^G b_l + a_{lm}^N$, where b_l are the frequency dependent beam transfer functions plotted in Fig. 12.

Figure 13 show the results of C_l^{2-1} plotted with respect to l for each frequency band. Similarly, Fig. 14 show the all

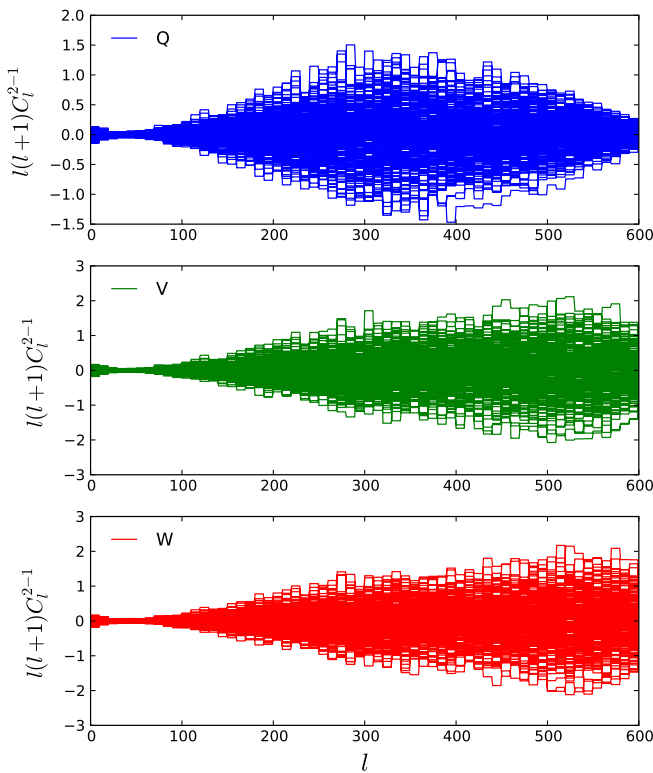


FIG. 13 (color online). The results for C_l^{2-1} from all 250 simulations for the three frequency bands. These plots have been binned with $\delta l = 10$.

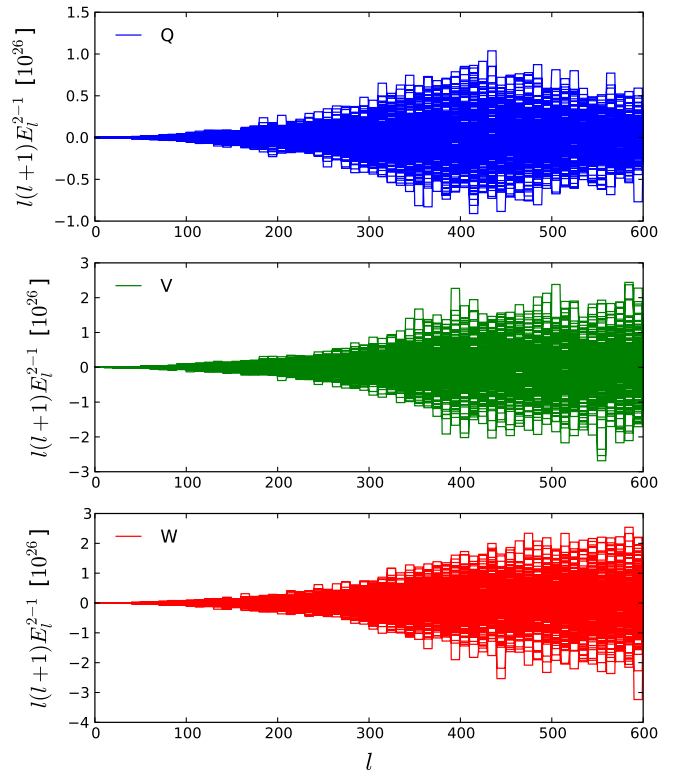


FIG. 14 (color online). The results for E_l^{2-1} from all 250 simulations for the three frequency bands. These plots have been binned with $\delta l = 10$.

250 simulated E_l^{2-1} plotted for each frequency band. These were binned with $\delta l = 10$.

From these 250 simulations, we are able to develop a covariance matrix that will be used for best-fit estimates with error bars. We find this covariance matrix by binning all 250 resulting estimators, C_l^{2-1} (or E_l^{2-1}), in bins of $\delta l = 40$. We can then treat each of these as an observation for each l bin and create the covariance matrix by calculating the covariance of these observations. This produced an $N \times N$ covariance matrix where N is the number of l bins.

Figure 15 shows the correlation matrices from the simulations. These matrices were obtained by taking the covariance matrix C_{ij} and building the correlation matrix \hat{C}_{ij} from the normalization

$$\hat{C}_{ij} = \frac{C_{ij}}{\sqrt{C_{ii}C_{jj}}}. \quad (47)$$

We see that the correlation matrix obtained from the C_l^{2-1} simulations show that these estimators have highly correlated l bins. It is interesting to note that the low l bins are highly correlated with each other, and the high l bins are highly correlated with each other but low l bins are not correlated strongly with the high l bins.

We also see correlation in the E_l^{2-1} estimators but not nearly to as great a degree as C_l^{2-1} above. Furthermore, in the bottom of Fig. 15, we see the full $C_l^{2-1} + E_l^{2-1}$ corre-

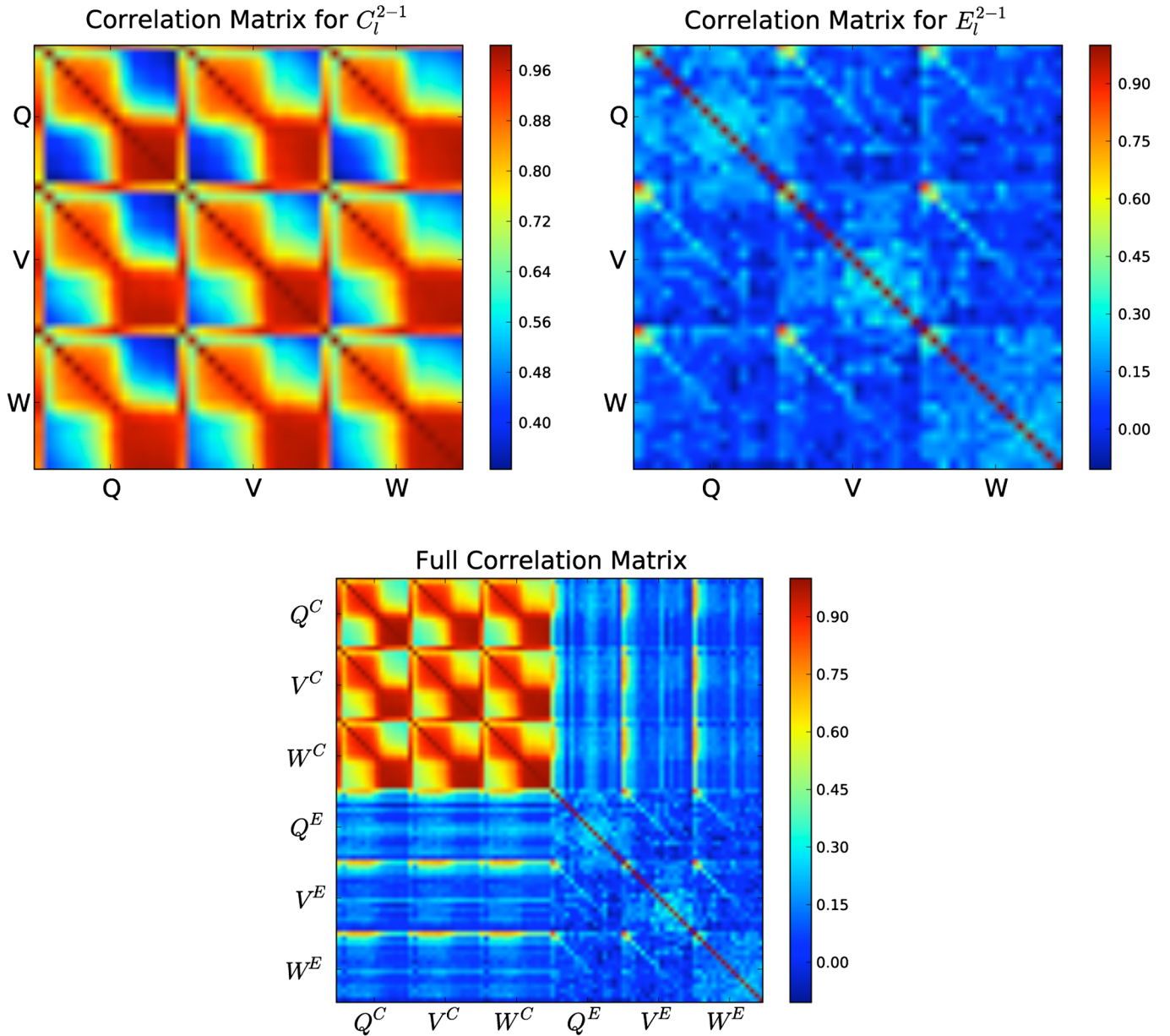


FIG. 15 (color online). Matrices showing correlations between each frequency for both C_l^{2-1} and E_l^{2-1} . The upper left hand corner shows correlations between small ell, and moving toward the lower right corner shows correlations between high ell.

lation matrix and note there is correlation between the l bins between C_l^{2-1} and E_l^{2-1} but not as much as there is between C_l^{2-1} alone.

C. Best-fit estimation

In order to fit the data, we use a least squares fitting analysis. Given a data set consisting of n points (x_i, y_i) , we can fit this data with a model function $f(\mathbf{x}, \mathbf{p})$ where there are m adjustable parameters held in the vector \mathbf{p} . We wish to find which of those parameter values best fit the data.

To do this, we minimize the χ^2 value defined as

$$\chi^2 = (\mathbf{y} - \mathbf{M} \cdot \mathbf{p})^T \mathbf{C}^{-1} (\mathbf{y} - \mathbf{M} \cdot \mathbf{p}), \quad (48)$$

where \mathbf{y} defines our data points we would like to fit to, \mathbf{p} are the parameters we wish to solve for, \mathbf{M} is a matrix containing our theoretical model we use for fitting, and \mathbf{C} is our covariance matrix described above.

For example, for a single frequency analysis where we would like to fit for f_{NL} and the coefficients for point sources: $\mathbf{y} = C_l^{2-1D}$ taken from data, \mathbf{M} is the vector containing $\langle C_l^{2-1 \text{Th}}, \text{PS}^{\text{Th}} \rangle$, and $\mathbf{p} = \langle f_{\text{NL}}, A_i \rangle$ with A_i being the coefficient for point sources.

We minimize χ^2 by setting its derivative to zero and solving for \mathbf{p} yielding

$$\mathbf{p} = (\mathbf{M}^T \mathbf{C}^{-1} \mathbf{M})^{-1} \mathbf{M}^T \mathbf{C}^{-1} \cdot \mathbf{y}. \quad (49)$$

TABLE II. Parameter estimates with C_l^{2-1} (top), E_l^{2-1} (middle), and the combination of the two (bottom) with Q , V , W , and $V + W$ maps for the case where we ignore point sources and including point sources. The point source amplitudes are listed under columns for A_i 's. The Q -band point source amplitude of $(24.2 \pm 5.0) \times 10^{-25}$ sr², equivalent to $(4.9 \pm 1.0) \times 10^{-5}$ $\mu\text{K}^3\text{-sr}^2$, is consistent with the WMAP team's preferred value of $(4.3 \pm 1.3) \times 10^{-5}$ $\mu\text{K}^3\text{-sr}^2$. The value of f_{NL} with the amplitude of point sources marginalized over 11.5 \pm 23.6.

Type	f_{NL} (no PSs)	f_{NL} (w/PSs)	A_Q	A_V	A_W	χ^2/dof
C_l^{2-1}						
Q	-61.6 ± 32.2	-10.5 ± 33.6	62.0 ± 12.1			1.6
V	5.4 ± 30.4	36.5 ± 32.9		22.1 ± 9.0		0.6
W	5.5 ± 30.0	31.8 ± 33.3			18.6 ± 10.1	0.6
$V + W$	4.8 ± 27.7	39.0 ± 30.7		18.5 ± 8.2	25.3 ± 9.2	1.0
E_l^{2-1}						
Q	426.4 ± 100.5	280.4 ± 111.3	17.7 ± 5.8			1.3
V	159.1 ± 98.0	107.3 ± 104.6		3.2 ± 2.3		0.3
W	90.4 ± 102.6	84.9 ± 108.6			0.4 ± 2.4	0.3
$V + W$	133.1 ± 140.9	102.4 ± 93.9		3.3 ± 2.2	-0.1 ± 2.3	0.8
Full						
Q	-23.1 ± 29.4	-22.0 ± 29.4	24.2 ± 5.0			3.2
V	13.1 ± 26.8	16.3 ± 26.8		4.2 ± 2.1		0.6
W	19.5 ± 26.9	19.5 ± 27.0			0.4 ± 2.3	0.6
$V + W$	11.4 ± 23.6	11.5 ± 23.6		5.0 ± 1.8	-1.8 ± 2.0	0.9

Lastly, we find the error bars for our best-fit parameters via

$$\Delta \mathbf{p}^2 = (\mathbf{M}^T \mathbf{C}^{-1} \mathbf{M})^{-1}, \quad (50)$$

where the diagonal of this matrix gives the variance of the parameters, and the χ^2 fit is given by Eq. (48).

V. RESULTS AND DISCUSSION

A. f_{NL} estimate

We now discuss the results of our analysis. The primordial and foreground non-Gaussianity parameter estimates are summarized in Table II for the case with and without point sources and in Table III for the case with both point sources and lensing-secondary correlation. For each of

TABLE III. Parameter estimates with C_l^{2-1} (top), E_l^{2-1} (middle), and the combination of the two (bottom) with Q , V , W , and $V + W$ maps for the case where we account for both point sources and the amplitude of lensing-secondary bispectrum. The point source amplitudes are listed under columns for A_i 's, while the amplitude of the lensing-secondary signal is tabulated under η_i 's. Our preferred value of f_{NL} with the amplitude of point sources and the lensing-secondary signal marginalized over using V and W maps in combination is 11.0 ± 23.7 .

Type	f_{NL} (PS + lensing)	A_Q	A_V	A_W	η_Q	η_V	η_W	χ^2/dof
C_l^{2-1}								
Q	21.1 ± 40.3	-80.2 ± 39.3			-11.7 ± 5.8			3.4
V	15.7 ± 38.9		8.7 ± 23.0			-3.7 ± 4.6		1.0
W	-13.5 ± 39.8			39.7 ± 25.6			0.6 ± 4.4	1.2
$V + W$	14.3 ± 37.6		18.2 ± 20.8	9.0 ± 22.0		-2.7 ± 4.1	-2.2 ± 4.0	1.3
E_l^{2-1}								
Q	122.2 ± 118.6	8.5 ± 6.2			6.6 ± 1.7			0.7
V	80.5 ± 107.8		2.1 ± 2.6			1.2 ± 1.1		0.3
W	62.3 ± 113.2			-0.2 ± 2.5			0.9 ± 1.3	0.3
$V + W$	72.0 ± 103.1		1.9 ± 2.4	-0.5 ± 2.4		1.4 ± 1.1	1.3 ± 1.2	0.8
Full								
Q	21.8 ± 29.6	24.0 ± 5.7			0.2 ± 1.2			3.3
V	16.7 ± 27.1		4.1 ± 2.4			0.2 ± 0.5		0.6
W	18.7 ± 27.2			0.5 ± 2.3			-0.3 ± 1.0	0.8
$V + W$	11.0 ± 23.7		2.8 ± 2.2	-0.4 ± 2.2		1.0 ± 0.8	-0.6 ± 0.9	0.9

these analyses, we bin and tabulate our measurements with bins of $\delta l = 40$. When $\delta l < 20$, the data are noisy to see the overall structure with a large covariance between adjacent bins and when $\delta l > 100$, information from the fluctuating point source curves is lost leading to a large degeneracy between parameters and an increase in parameter errors. Furthermore, of all binning widths between $20 < \delta l < 100$, the results are similar, but the best χ^2 value is always found with a binning at $\delta l = 40$ (Fig. 16). Note that in the limit of a large δl bin (with $\delta l > 200$), we effectively reach the case of determining f_{NL} similar to the previous skewness statistic, with effectively just one data point per band.

In Tables II and III the first set of results, denoted by C_l^{2-1} , show the case when we fit our measured C_l^{2-1} to the theoretical predictions involving a combination of primordial non-Gaussianity, point sources, and lensing correlations as shown in Fig. 2. Given that Q map leads to a poor χ^2 when model fitting Q alone or Q in combination with other maps, we exclude the $Q + V + W$ combination and instead consider $V + W$ as our preferred set of maps. When fitting to V and W , we compute the covariance of V and W , for example $\langle C_l^{2-1,V} C_l^{2-1,W} \rangle - \langle C_l^{2-1,V} \rangle \langle C_l^{2-1,W} \rangle$. Without point sources and lensing and simply fitting to f_{NL} with C_l^{2-1} , we find 4.8 ± 27.7 .³ If the shot-noise from point sources are included, after marginalizing over A_V and A_W , we find $f_{\text{NL}} = 39.0 \pm 30.7$.

As we discussed earlier, however, fitting to C_l^{2-1} alone with point sources lead to a worse determination of f_{NL} than in the case where point sources are ignored due to the degeneracy between primordial non-Gaussianity and point sources. Thus, we also include E maps in our analysis with the associated results from the skewness power spectrum denoted with E_l^{2-1} in Tables II and III. The E maps provide a better estimator for the point sources but a worse estimator for f_{NL} than the C_l^{2-1} estimator, for reasons we discussed already. (Figure 3) With E_l^{2-1} , the error bars for the point source amplitudes are about half of what they were for C_l^{2-1} alone; whereas, the error bars on f_{NL} are about 3 times worse.

One interesting thing to note is that E_l^{2-1} is always positive. This shows up in the best-fit f_{NL} values, where for C_l^{2-1} only the Q map pushes f_{NL} towards a negative value; whereas, E_l^{2-1} from Q pushes f_{NL} to a large positive value. In fact, if we include Q band and do an f_{NL} analysis with the E map alone, we find a 6σ detection of the primordial non-Gaussianity. The χ^2 from such an analysis, however, is poor and the result should not be trusted as a detection of a nonzero f_{NL} .

Finally, we consider the best fit when C_l^{2-1} and E_l^{2-1} are combined. The $V + W$ analysis gives us the best constraint on f_{NL} with $-36.4 < f_{\text{NL}} < 58.4$ at the 95% confidence level or (11.0 ± 23.7) at the 68% confidence level, when

³We quote 1σ results with \pm error and 2σ result as a range.

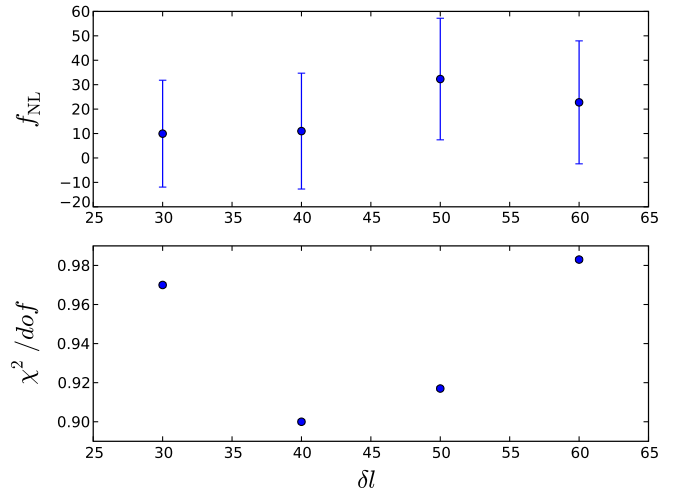


FIG. 16 (color online). The various f_{NL} values taken from various binnings of the data from a full analysis considering both C_l^{2-1} and E_l^{2-1} with point sources and ISW.

we include both point sources and the lensing-secondary correlation and marginalize over $(A_V, A_W, \eta_V, \eta_W)$. As with the C_l^{2-1} only analysis, this combined analysis has f_{NL} consistent with zero at 1σ . As seen by comparing Tables II and III in the $V + W$ case, our f_{NL} is essentially the same whether we include the lensing-secondary bispectrum or not.

While we do not include the Q band in our f_{NL} estimate, the Q -band point source amplitude of $(24.2 \pm 5.0) \times 10^{-25} \text{ sr}^2$ using the combination of C_l^{2-1} and E_l^{2-1} is consistent with the WMAP team's preferred value for the point source amplitude of $(4.3 \pm 1.3) \times 10^{-5} \mu\text{K}^3\text{-sr}^2$ [12]. In their units, our b_{PS}^Q is equivalent to $(4.9 \pm 1.0) \times 10^{-5} \mu\text{K}^3\text{-sr}^2$. While we cannot make an exact comparison as the WMAP team tabulates their point source values with l_{max} of 900, our values for b_{PS}^V and b_{PS}^W are also within uncertainties consistent with previous measurements. While the non-Gaussianity associated with point sources is detected, we do not detect the lensing-secondary bispectrum. It is likely that the C_l^{2-1} and E_l^{2-1} are not the best ways to detect this correlation. The best-fit values for η_V and η_W , however, are close to their 1σ errors.

As tabulated in Table III, including the bispectrum of lensing-secondary correlations does not lead to a significant degradation of the f_{NL} measurement. We find $f_{\text{NL}} = 11.0 \pm 23.7$ at the 1σ confidence level, but we do not find a detection of η_i in each of the three bands when C_l^{2-1} is combined with E_l^{2-1} .

Note that our $V + W$ analysis gives an f_{NL} value fully consistent with zero at the 1σ level. Previous results have suggested a marginal hint of a primordial non-Gaussianity with the most recent optimal analysis giving $f_{\text{NL}} = 38 \pm 21$ [40] (Table IV). Compared to this result, our $V + W$ has a slightly worse error with 11.0 ± 23.7 , and the increase of 13% is consistent with the fact that our analysis is sub-

TABLE IV. Summary of recent results on f_{NL} measurements. Compared to the expectation from Cramer-Rao bound using the Fisher matrix estimate, our measurement is suboptimal, but compared to the previous best estimate for f_{NL} of 38 ± 21 , our estimate is fully consistent with zero at the 1σ confidence level.

Technique	f_{NL}	Ref.
WMAP 3-year, skewness	87 ± 30	[39]
WMAP 5-year, skewness	51 ± 30	[12]
WMAP 5-year, Minkowski functions	-57 ± 61	[12]
WMAP 5-year, wavelets	31 ± 24.5	[67]
WMAP 5-year, needlets	84 ± 40	[68]
WMAP 5-year, needlets northern hemisphere	-25 ± 75	[69]
WMAP 5-year, needlets southern hemisphere	75 ± 75	[69]
WMAP 5-year, N -point probability distribution function	30 ± 62	[70]
WMAP ISW correlation	236 ± 127	[71]
Large-scale structure bias	20.5 ± 24.8	[72]
WMAP 5-year, optimal estimator	38 ± 21	[40]
WMAP 5-year, skew-power spectrum	$11.0 \pm 23.7(\pm 1.5)$	this paper

optimal. As discussed earlier, however, our approach is not different from both the WMAP team's approach [12] and previous other estimates of f_{NL} [39]. Moreover, our l_{max} is set at 600, while their analysis extends to 750.

Furthermore, it is interesting to note what tight constraints the E maps place on the parameters. In Fig. 17, we see that E_l^{2-1} places a very tight fit on the best-fit point source coefficients. For example, this fit is tight enough that the best overall f_{NL} midpoint value is pulled down from 39.0 using C_l^{2-1} only with point sources to 11.5 for the full analysis. The E map analysis is thus nontrivial indeed.

To see if there is any scale dependence to non-Gaussianity, we bin f_{NL} in widths of 200 and estimate the value between $0 < l < 600$. The results are shown in Fig. 18 and tabulated in Table V. Except in the last bin for the case with point sources only between $400 < l < 600$, our f_{NL} values are fully consistent with zero at the 1σ level and the last bin is consistent with zero at the 2σ level. The last bin also has a large error due to the increase of the instrumental noise. For the same reason, we do not pursue a measurement of f_{NL} when $l > 600$.

It is also interesting to note how accurate our overall error estimate is. As we compute our covariances with 250 simulations, there is an inherent error of $1/\sqrt{250}$ in the error bars we obtained in this analysis. Because of this, we note that a more accurate estimate of f_{NL} should be to consider it as $11.0 \pm 23.7(\pm 1.5)$, where the extra error within the bracket denotes an additional statistical error associated with the finite number of simulations.

B. Cross skewness

Previous results for f_{NL} from the WMAP 5-year team compute f_{NL} by compressing all information into a single quantity called cross skewness defined by Eq. (26). To compare our measurement C_l^{2-1} with their results, we

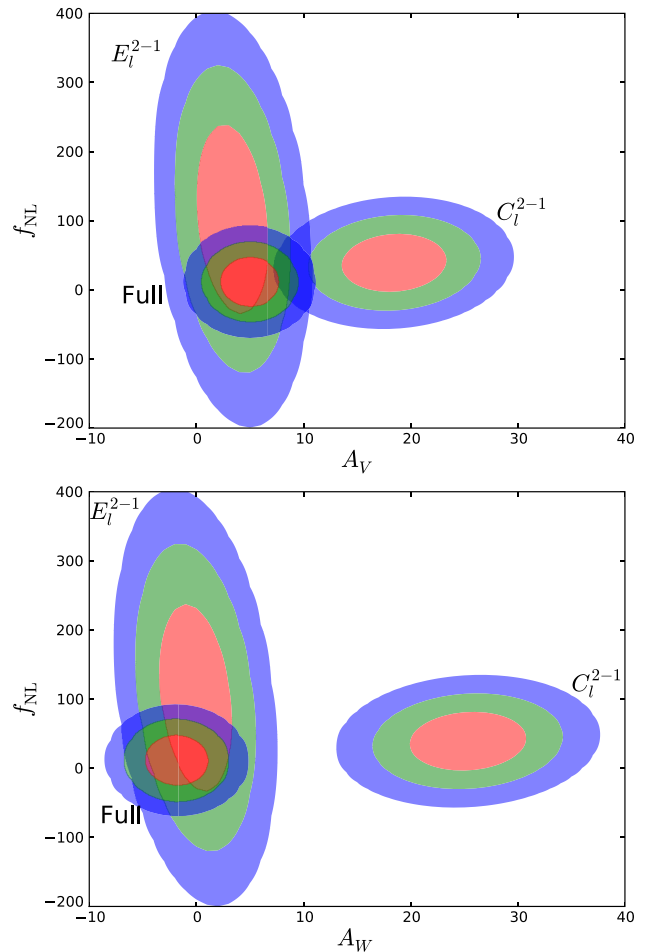


FIG. 17 (color online). Top: Confidence intervals showing constraints on f_{NL} versus A_V for the C_l^{2-1} , E_l^{2-1} , and full analysis. Below: Same for A_W . Red is 68% confidence interval (CI), Green is 95% CI, and blue is 99.7 CI.

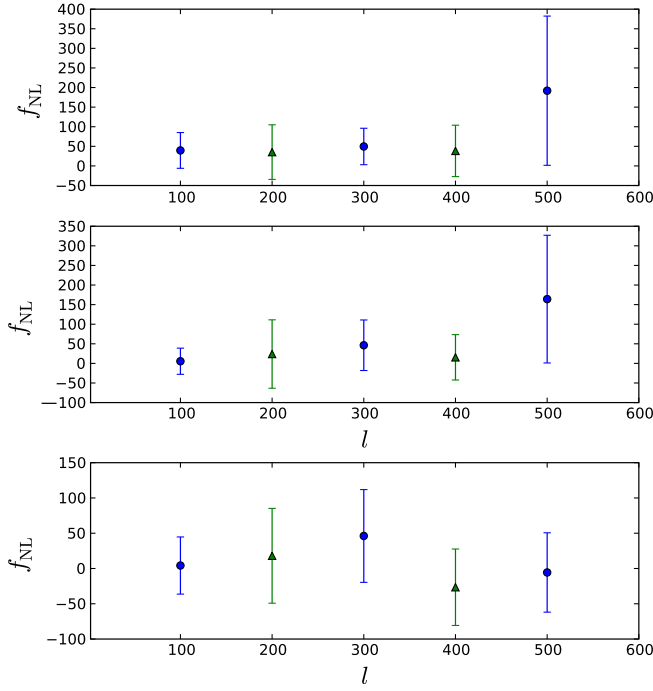


FIG. 18 (color online). Angular dependence of f_{NL} between $2 < l < 600$ in bins of 200. The top panel is for C_l^{2-1} only and with point sources. The middle panel is the full measurement with C_l^{2-1} and E_l^{2-1} and using point sources. The lower panel is full measurement with both point sources and lensing-secondary correlations. The blue circles use mutually disjoint bins from each other. The green triangles also use mutually disjoint bins.

calculate our own equivalent version of this cross skewness statistic defined as

$$\hat{S}_{AB^2} = \sum (2l+1) C_l^{2-1,D}, \quad (51)$$

where $C_l^{2-1,D}$ is the estimator obtained from data. We also compute the skewness of the E map using $E_l^{2-1,D}$ in above.

TABLE V. Independent estimates of f_{NL} in bins of $\delta l = 200$ between $2 < l < 600$.

Type	f_{NL} (with PSs)	f_{NL} (PSs + lensing-secondary)
C_l^{2-1}		
$2 < l < 200$	39.5 ± 45.6	5.5 ± 33.4
$100 < l < 300$	35.3 ± 69.6	23.9 ± 87.3
$200 < l < 400$	49.6 ± 46.5	46.3 ± 64.5
$300 < l < 500$	38.3 ± 65.6	15.5 ± 57.8
$400 < l < 600$	192.0 ± 190.4	164.1 ± 162.9
Full		
$2 < l < 200$	-9.2246 ± 44.6	4.2 ± 40.5
$100 < l < 300$	-6.1 ± 101.4	18.0 ± 67.2
$200 < l < 400$	64.5 ± 74.0	46.1 ± 65.8
$300 < l < 500$	68.3 ± 92.8	-26.5 ± 54.2
$400 < l < 600$	103.6 ± 178.3	-5.6 ± 56.3

We jointly fit \hat{S}_{AB^2} and \hat{S}_{E^3} with a combination of f_{NL} and A_i by effectively comparing the statistic from data to prediction from theory with theory expectation computed as, for example, $S_{AB^2} = \sum (2l+1) C_l^{2-1,\text{Th}}$. In order to determine the errors, we also preform the same cross-skewness analysis on all 250 simulations and calculate the covariance of \hat{S}_{AB^2} and \hat{S}_{E^3} from these 250 numbers for each frequency. We find that f_{NL} estimated from each of the 250 Gaussian and noise simulations leads to a Gaussian error distribution (Fig. 19).

We tabulate our results for f_{NL} after marginalizing over A_i 's in Table VI. Here, when doing the summations, we set $l_{\text{max}} = 500$ so we can compare directly with WMAP 5-year published results [12]. We see that for all three channels, we have good agreement with the WMAP team's 5-year findings. Our best-fit value tends to be bit more positive than quoted by the WMAP team (with 0.26σ , 0.25σ , 0.17σ in Q , V , and W , respectively), but this is a small difference when compared to the large error bar. The errors quoted in the WMAP 5-year paper are consistent with our measurements had we used the skewness statistic. However, as we discussed earlier, fitting to C_l^{2-1} and E_l^{2-1} leads to an improvement in the error estimate of

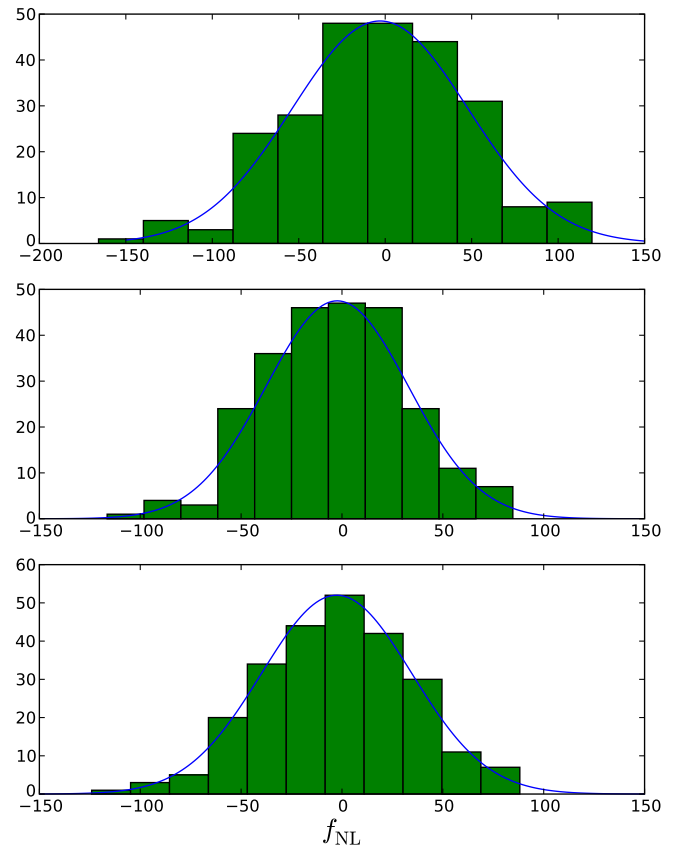


FIG. 19 (color online). Histogram of the f_{NL} estimated from Gaussian and noise simulations for the cross-skewness statistic $S_3 = \sum (2l+1) C_l^{2-1}$. Top: Q , Middle: V , Bottom: W . A best-fit Gaussian curve is plotted in blue over each histogram.

TABLE VI. Summary of results using the skewness where $S = \sum(2l+1)C_l^{-2}$. Here, we tabulate the values found in our analysis and the ones reported by the WMAP team [12]. We set $l_{\max} = 500$ here.

Band	f_{NL}	WMAP 5-year
Q	-27.3 ± 50.8	-42 ± 48
V	52.0 ± 35.2	41 ± 35
W	50.5 ± 37.3	46 ± 35

f_{NL} , since the shapes of the two skew spectra allow us to break the degeneracies better. Comparing our $V + W$ result using the two spectra to skewness for the same maps, we find that the improvement in the error is roughly 20%.

VI. CONCLUSION

In this paper, we constrained the primordial non-Gaussianity parameter of the local model f_{NL} using the skewness power spectrum associated with the two-to-one cumulant correlator of cosmic microwave background temperature anisotropies. This bispectrum-related skewness power spectrum was constructed after weighting the temperature maps with the appropriate window functions to form an estimator that probes the multipolar dependence

of the underlying bispectrum associated with primordial non-Gaussianity.

We also estimate a separate skewness power spectrum more sensitive to unresolved point sources. When compared to previous attempts at measuring the primordial non-Gaussianity with WMAP data, our estimators have the main advantage that we do not collapse information to a single number. When model fitting two-to-one skewness power spectrum, we make use of bispectra generated by primordial non-Gaussianity, radio point sources, and lensing-secondary correlations.

We analyze Q , V , and W -band WMAP 5-year data using the KQ75 mask out to $l_{\max} = 600$. Using V - and W -band data and marginalizing over model parameters related to point sources, our overall and preferred constraint on f_{NL} is 11.0 ± 23.7 at the 68% confidence level ($-36.4 < f_{\text{NL}} < 58.4$ at 95% confidence). Despite previous claims, we find no evidence for a nonzero value of f_{NL} even marginally at the 1σ level.

ACKNOWLEDGMENTS

We are grateful to Eiichiro Komatsu, Dipak Munshi, and Kendrick Smith for assistance during various stages of this work.. Partial funding of A. A. and P. S. was from NSF CAREER Grant No. AST-0645427.

-
- [1] A. H. Guth, Phys. Rev. D **23**, 347 (1981).
 - [2] A. D. Linde, Phys. Lett. **108B**, 389 (1982).
 - [3] A. J. Albrecht and P. J. Steinhardt, Phys. Rev. Lett. **48**, 1220 (1982).
 - [4] K. Sato, Mon. Not. R. Astron. Soc. **195**, 467 (1981).
 - [5] D. Kazanas, Astrophys. J. **241**, L59 (1980).
 - [6] A. A. Starobinsky, JETP Lett. **30**, 682 (1979).
 - [7] A. H. Guth and S. Y. Pi, Phys. Rev. Lett. **49**, 1110 (1982).
 - [8] J. M. Bardeen, P. J. Steinhardt, and M. S. Turner, Phys. Rev. D **28**, 679 (1983).
 - [9] S. W. Hawking, Phys. Lett. **115B**, 295 (1982).
 - [10] V. F. Mukhanov, H. A. Feldman, and R. H. Brandenberger, Phys. Rep. **215**, 203 (1992).
 - [11] A. A. Starobinsky, Phys. Lett. **117B**, 175 (1982).
 - [12] E. Komatsu *et al.* (WMAP Collaboration), Astrophys. J. Suppl. Ser. **180**, 330 (2009).
 - [13] D. Baumann *et al.* (CMBPol Study Team Collaboration), AIP Conf. Proc. **1141**, 10 (2009).
 - [14] L. F. Abbott and M. B. Wise, Astrophys. J. **282**, L47 (1984).
 - [15] L. P. Grishchuk, Zh. Eksp. Teor. Fiz. **67**, 825 (1974) [Sov. Phys. JETP **40**, 409 (1975)].
 - [16] Planck Collaboration, arXiv:astro-ph/0604069.
 - [17] J. Bock *et al.*, arXiv:astro-ph/0604101.
 - [18] J. Bock *et al.* (EPIC Collaboration), arXiv:0906.1188.
 - [19] J. Bock *et al.*, arXiv:0805.4207.
 - [20] D. Baumann *et al.* (CMBPol Study Team Collaboration), AIP Conf. Proc. **1141**, 3 (2009).
 - [21] J. M. Maldacena, J. High Energy Phys. 05 (2003) 013.
 - [22] M. Sasaki and E. D. Stewart, Prog. Theor. Phys. **95**, 71 (1996).
 - [23] D. H. Lyth, K. A. Malik, and M. Sasaki, J. Cosmol. Astropart. Phys. 05 (2005) 004.
 - [24] D. H. Lyth and Y. Rodriguez, Phys. Rev. Lett. **95**, 121302 (2005).
 - [25] V. Acquaviva, N. Bartolo, S. Matarrese, and A. Riotto, Nucl. Phys. **B667**, 119 (2003).
 - [26] T. J. Allen, B. Grinstein, and M. B. Wise, Phys. Lett. B **197**, 66 (1987).
 - [27] T. Falk, R. Rangarajan, and M. Srednicki, Astrophys. J. **403**, L1 (1993).
 - [28] D. S. Salopek and J. R. Bond, Phys. Rev. D **42**, 3936 (1990).
 - [29] A. Gangui, F. Lucchin, S. Matarrese, and S. Mollerach, Astrophys. J. **430**, 447 (1994).
 - [30] S. Mollerach, Phys. Rev. D **42**, 313 (1990).
 - [31] G. Dvali, A. Gruzinov, and M. Zaldarriaga, Phys. Rev. D **69**, 023505 (2004).
 - [32] A. D. Linde, Pis'ma Zh. Eksp. Teor. Fiz. **40**, 496 (1984) [JETP Lett. **40**, 1333 (1984)].
 - [33] A. Berera, Phys. Rev. Lett. **75**, 3218 (1995).
 - [34] N. Arkani-Hamed, H. C. Cheng, M. A. Luty, and S. Mukohyama, J. High Energy Phys. 05 (2004) 074.
 - [35] E. Silverstein and D. Tong, Phys. Rev. D **70**, 103505

- (2004).
- [36] X. Chen, Phys. Rev. D **72**, 123518 (2005).
- [37] N. Bartolo, E. Komatsu, S. Matarrese, and A. Riotto, Phys. Rep. **402**, 103 (2004).
- [38] E. Komatsu and D.N. Spergel, Phys. Rev. D **63**, 063002 (2001).
- [39] A.P.S. Yadav and B.D. Wandelt, Phys. Rev. Lett. **100**, 181301 (2008).
- [40] K.M. Smith, L. Senatore, and M. Zaldarriaga, J. Cosmol. Astropart. Phys. 09 (2009) 006.
- [41] P. Serra and A. Cooray, Phys. Rev. D **77**, 107305 (2008).
- [42] A. Cooray, Phys. Rev. D **64**, 043516 (2001).
- [43] D. Munshi and A. Heavens, arXiv:0904.4478.
- [44] D.M. Goldberg and D.N. Spergel, Phys. Rev. D **59**, 103002 (1999).
- [45] A. Cooray and W. Hu, Astrophys. J. **548**, 7 (2001).
- [46] G. Hinshaw, A.J. Banday, C.L. Bennett, K.M. Gorski, and A. Kogut, Astrophys. J. **446**, L67 (1995).
- [47] P.G. Ferreira, J. Magueijo, and K.M. Gorski, Astrophys. J. **503**, L1 (1998); for updates, see also, J. Pando, D. Vallas-Gabaud, and L. Fang, Phys. Rev. Lett. **81**, 4568 (1998); A. J. Banday, S. Zaroubi, and K. M. Gorski, arXiv: astro-ph/9908070 [Astrophys. J. (to be published)]; B. Bromley and M. Tegmark, Astrophys. J. Lett. **524**, L79 (1999).
- [48] A. Cooray, W. Hu, and M. Tegmark, Astrophys. J. **540**, 1 (2000).
- [49] U. Seljak and M. Zaldarriaga, Astrophys. J. **469**, 437 (1996).
- [50] P. Serra, A. Cooray, A. Amblard, L. Pagano, and A. Melchiorri, Phys. Rev. D **78**, 043004 (2008).
- [51] D. Munshi, P. Valageas, A. Cooray, and A. Heavens, arXiv:0907.3229.
- [52] A. Cooray and R.K. Sheth, Phys. Rep. **372**, 1 (2002).
- [53] A. Cooray, Phys. Rev. D **62**, 103506 (2000).
- [54] A. Cooray, Phys. Rev. D **64**, 063514 (2001).
- [55] A. Cooray, Phys. Rev. D **65**, 103510 (2002).
- [56] N. Afshordi, Phys. Rev. D **70**, 083536 (2004).
- [57] E. Komatsu and U. Seljak, Mon. Not. R. Astron. Soc. **336**, 1256 (2002).
- [58] A. Mangilli and L. Verde, arXiv:0906.2317 [Phys. Rev. D (to be published)].
- [59] D. Hanson, K.M. Smith, A. Challinor, and M. Liguori, Phys. Rev. D **80**, 083004 (2009).
- [60] A. Cooray, D. Sarkar, and P. Serra, Phys. Rev. D **77**, 123006 (2008).
- [61] M. Veneziani *et al.*, Astrophys. J. **702**, L61 (2009).
- [62] G. Chen and I. Szapudi, Astrophys. J. **647**, L87 (2006).
- [63] E. Komatsu, D.N. Spergel, and B.D. Wandelt, Astrophys. J. **634**, 14 (2005).
- [64] K. M. Gorski, E. Hivon, A. J. Banday, B. D. Wandelt, F. K. Hansen, M. Reinecke, and M. Bartelman, Astrophys. J. **622**, 759 (2005).
- [65] N. Jarosik *et al.* (WMAP Collaboration), Astrophys. J. Suppl. Ser. **170**, 263 (2007).
- [66] G. Hinshaw *et al.* (WMAP Collaboration), Astrophys. J. Suppl. Ser. **180**, 225 (2009).
- [67] A. Curto, E. Martinez-Gonzalez, and R.B. Barreiro, Astrophys. J. **706**, 399 (2009).
- [68] O. Rudjord, F.K. Hansen, X. Lan, M. Liguori, D. Marinucci, and S. Matarrese, Astrophys. J. **701**, 369 (2009).
- [69] D. Pietrobon, P. Cabella, A. Balbi, R. Crittenden, G. de Gasperis, and N. Vittorio, arXiv:0905.3702.
- [70] P. Vielva and J.L. Sanz, arXiv:0812.1756 [Mon. Not. R. Astron. Soc. (to be published)].
- [71] N. Afshordi and A.J. Tolley, Phys. Rev. D **78**, 123507 (2008).
- [72] A. Slosar, C. Hirata, U. Seljak, S. Ho, and N. Padmanabhan, J. Cosmol. Astropart. Phys. 08 (2008) 031.